5 | Modified Bilayer of g-C_3N_4

In this chapter, We discuss the importance of interlayer coupling governed by the interlayer atomic superposition. Specifically, we elaborate on the structural, electronic, optical, and photocatalytic properties of nine spatially modified bilayers of CN in the backdrop of existing relevant literature. We will discuss the dependence of the π-localization effects of planar/corrugated geometry of the bilayer over the overpotential of the HER and OER. Li was intercalated in the most effective bilayer configuration to improve the interlayer charge transfer channel. A qualitative discussion of the band structures and simultaneous OER and HER is presented in conjunction with the synergistic effect of the interlayer ($\vec{E_{il}}$) and interfacial ($\vec{E_{if}}$) electric fields produced by the partial charge migration through Li-atom along with associated reaction intermediates on the photocatalytic activity. This is followed by the quantitative analysis of the charge transfer mechanism through charge density variation. For the enhanced photocatalytic activity of Li-CN, the accompanying investigation demonstrates the mutual interplay of $\vec{E_{il}}$, $\vec{E_{if}}$, and the adsorption energy of reaction adsorbates.

5.1 The Case of Bilayer-g-C_3N_4

In addition to demonstrating an exponential increase in hydrogen production, dye degradation, overall water splitting, nitrogen reduction, and carbon dioxide reduction to hydrocarbon fuel, functionalization of the CN along with decreasing dimensionality has opened up new areas of interest. Such as homojunction and various types of heterojunction formation for improving photocatalytic activity as well as its multifunctional applications through possible combinations of diverse materials that may have synergistic effects [124]. The forbidden energy gap increases as the material gets closer to reduced dimensionality due to the quantum confinement effect, although charge redistribution and increased planar and inter-planar charge carrier mobility are caused by the separation of stacked layers. Wei et al.' [125] investigation on the CN monolayer with quasi-particle correction shows that band gap tuning set up by excitonic absorption adjusts for the dimensionality of the material and results in better electron-electron correlation and higher solar energy conversion efficiency [125]. The topological shift in CN brought about by interstitial and substitutional doping modifies connection patterns and results in high activity, suggesting a synergistic impact of dopant properties and structural changes [126]. The major role of tri-s-triazine-based material in the race of metal-free photocatalysts has been confirmed by subsequent theoretical and experimental investigation on the stability and photocatalytic activity of structurally modified layered CN based on the interlayer orbital coupling and energetically most stable configuration. By avoiding the repulsive interaction between nitrogen lone pairs (LP), Gracia et al.'s [127] initial investigation utilizing *ab-initio* molecular dynamics showed the stability of layered arrangement, resulting in the production of a corrugated yet low-energy structure *via* using a planar and stable corrugated monolayer arrangement with nitrogen LP positioned above the structural holes to reduce repulsion and improve the catalytic performance of CO/CH_3OH via distorted geometry, Azofra et al. [99] have studied the carbon dioxide reduction process. To get a greater understanding of interlayer coupling and their visible light response, bilayers were explored in 16 distinct configurations.

These configurations included stacking nitrogen that was bridged and edged over one another as well as various alignment patterns [100]. Its application in photovoltaic materials was limited by its increased band gap and visible light absorption when compared to monolayers. In contrast, a study on stable structures based on excitonic effect and stacking ranges from monolayer to four layers was conducted for the HER, solely taking into account ABAB stacking. When working with polyfunctional material in bulk form, Wang et al. [128, 129] and Zuluaga and associates [130] talked about off-plane distortion and interlayer stacking arrangements as potential explanations for differences in band gap tuning and experimental lattice parameters. Excitonic perspective revealed a broadening of the absorption region as a result of the electron-hole pair localization at reactive sites, the electronic transition channel around Fermi being activated, and the transformation of dark excitation to bright excitation, which weakens the N-H bond and facilitates an efficient HER [131]. Ultimately, a two-step ultrasonication-calcination synthesis technique that produced carbon nitride nanosheets demonstrated the enhanced HER efficiency by electron transport via tunneling between vertically aligned C-N pairs. An indirect association between the band gap of CN and the synthesis temperature was shown by the hybridization and overlap of p_z states [132].
Li et al. [133] have described the following techniques for controlling the behavior of photo-excited electron-hole pairs to achieve effective separation, high mobility, and an increase in recovery time. i. heterojunction production; ii. catalyst spin polarization regulation; iii. donor-acceptor system design by doping and decorating; and iv. functionalization-induced exciton generation. On the other hand, modifying and composing CN into a bilayer is another method for creating photocatalysts with highly active sites and the desired surface reactivity. This can assist in solving the issue of photogenerated charge carrier separation and transfer, which lowers the rate of recombination and increases the recovery time by offering a wide window for oxidation and reduction reactions. Even with research on specific photocatalytic reaction pathways, there is still a lack of understanding of the OER, the C-N interlayer interaction, and how these factors affect the change in HER efficiency with water molecules. In the current situation, it is essential

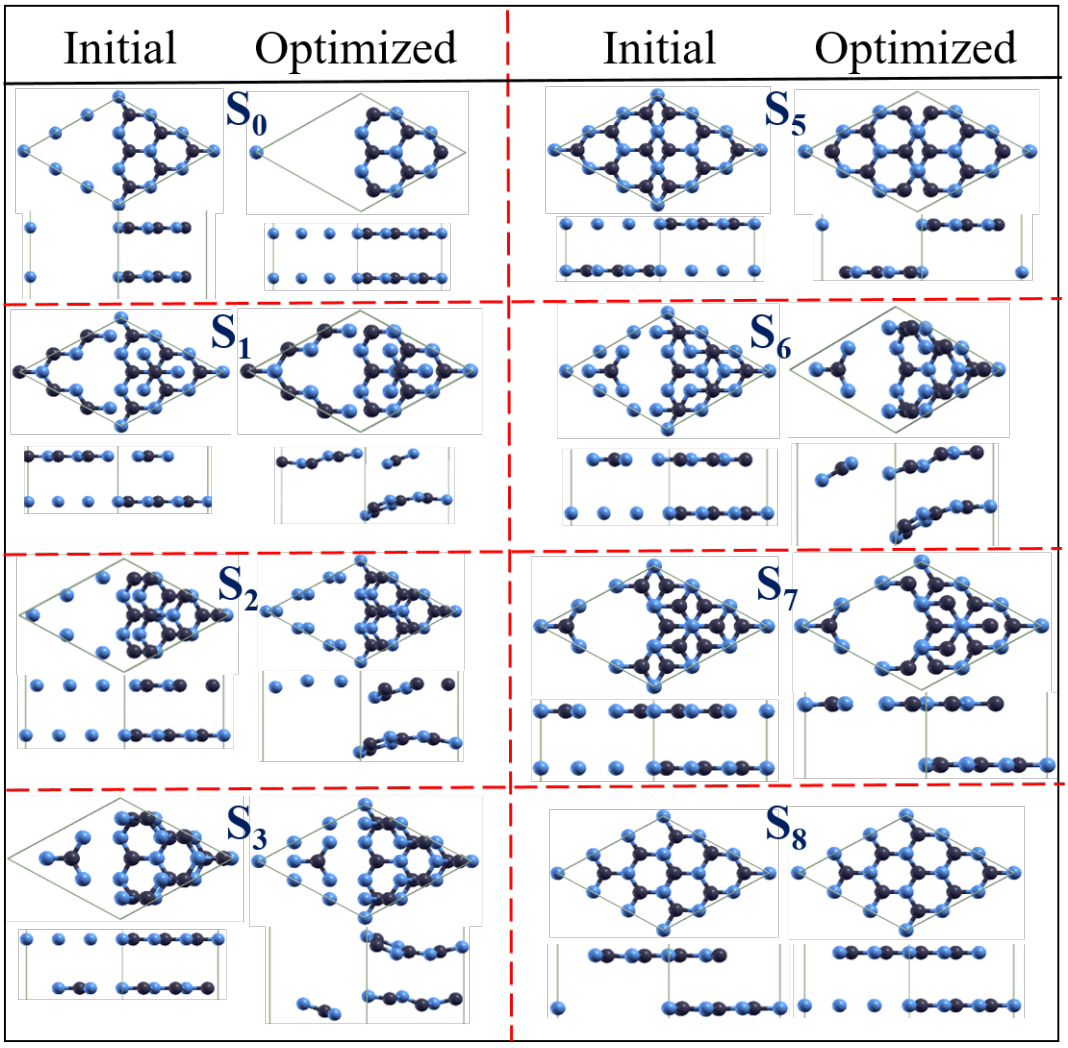

FIGURE 5.1: Initial and optimized structure in top and side configuration has been demonstrated for $S_0 - S_8$ bilayer arrangement of CN.

to investigate the possibilities of stable structural change and how it affects the dynamics of photogenerated charge carriers for future development and knowledge at a macroscopic level for investigating mechanisms.

The present study examines the function of interlayer orbital interaction and π-conjugation in the formation of stable CN bilayers, taking into account the potential for bi/tri bonded N-N, C-C, and N-C orbitals. In terms of low Gibbs free energy and overpotential values, its electronic and optical characteristics as well as the formation of active reaction sites for photocatalytic OER and HER are demonstrated. This also clarified why enhanced photocatalytic activity was achieved in comparison to a CN monolayer, based on the generation of an $\vec{E_{if}}$ as a result of charge transfer as the intermediate radicals adsorbed over the surface.

5.2 *BL-CN* Computational Details and Models

The electronic and optical properties of the system were determined using Hybrid DFT, which was implemented in the Quantum Espresso code [76]. The HSE06 [60, 61] functional was used for accurate band gap calculations, while the PBE-GGA [58] was used to compute the structural and thermodynamical properties. To produce a band gap value similar to earlier research, the screening parameter within the limit ($\omega < 0.15a_0^{-1}$) is assumed to be $\omega = 0.046a_0^{-1}$. All calculations are performed using ONCV with plane waves-based basis sets cutoff for the kinetic energy of 60 Ry taken into consideration following a systematic convergence test for the system's total energy to mimic all-electron outcomes with high accuracy. Grimme-D2 [70] correction has been used to incorporate dispersion correction to the total energy for vdW interaction within the bilayer. A uniform $3 \times 3 \times 3$ grid was employed to calculate the costlier hybrid functional-based characteristics, whereas a Γ centered $5 \times 5 \times 2$ Monkhorst-Pack k point grid was used for structural and thermodynamic calculations. Self-consistent field iterations were used to carry out the electronic optimization, with an energy cutoff of $10^{-6} a.u.$, and a force convergence threshold of 10^{-3} a.u./Å per atom for the relaxation of atomic positions and the unit cell. XCrySDen [91] software is used to visually investigate various forms of the bilayer.

With a vacuum of $\approx$ 16 Å and an interlayer distance of 3.275 Å, we have taken into consideration the unit cell of lattice parameter 7.14 Å for both monolayer (ML) and bilayer studies. Additionally, we have isolated layers in 2D to truncate the Coulomb interaction in the z direction thereof, thereby eliminating any interaction with the next periodic layer in the case of bilayer structures, which consist of a total of 28 atoms (16 N + 12 C). To investigate the kind of viable atomic orbital alignment in vertical layer stacking, the various bilayer structures, namely S_0, S_1, S_2, S_3, S_4, S_5, S_6, S_7, and S_8, are taken into consideration based on interlayer atomic/bond alignment. These structures, denoted as S_0, S_1, S_2, and S_8, are AA (without rotation) stacked structures. S_0 represents the bilayer in which the tri-s-triazine moieties are exactly over each other; for S_1, the upper layer (UL) is

displaced to align bay carbon (C^{bay}) over the 3-fold coordinated (N^{tri}) hybridized N of the lower layer (LL); for S_2, the UL is positioned so that the atoms of UL align over the bonds of LL; and for S_8, N^{tri} lie over the void of LL and similar atoms over each other. While the remaining structures, S_3, S_4, S_5, S_6, and S_7, are AB stacked with UL rotated 180° for LL, S_3 displays the position of N^{tri} of UL over the void of LL and C atoms align over N atoms; in S_4, the UL is slightly displaced along the xy plane compared to S_3, but with atoms aligned over the bonds; S_5 consists of least direct atomic alignment with N^{edge} of both layer aligned over each other; S_6 includes alignment of N atoms over the hexagon pore while C atom aligns with C of either layer and S_7 displays the alignment of similar N atoms of both layers over each other. Cohesive energy (Δ_{Coh}) is computed for each of the bilayers (S_0–S_8) to assess the interlayer bonding strength and structural stability using:

$$\Delta_{Coh} = E_{BL} - 2 \times E_{ML} \tag{5.1}$$

where E_{BL} and E_{ML} are the total energy of the respective bilayer and ML. We have utilized the technique established by Nørskov and colleagues [73–75], which includes the computation of Gibbs free energy (ΔG) preceded by the adsorption energy of intermediates, as previously mentioned, to study the single electron transfer step of HER and the four-electron transfer mechanism for OER. Together with the revised ΔG equation by Nørskov et al. [73–75], the single electron transfer step of Volmer-Heyrovsky [134] for HER is employed, with n = 0 indicating an isolated hydrogen atom adsorbed over the surface and n = 1 signifying the influence of an additional water molecule.

$$[(H_2O)_n + H^+] + e^- \longrightarrow *H + (H_2O)_n \tag{5.2}$$

$$[(H_2O)_n + H^+] + *H + e^- \longrightarrow H_2 + (H_2O)_n \tag{5.3}$$

$$\Delta G_{*H} = \Delta E_{*H} + 0.24 \tag{5.4}$$

For the computation of ΔG, an adjustment based on the impact of the additional water molecules is made appropriately.

5.3 BL-CN Structural and Electronic Properties

A spatially modified bilayer with various layered alignments has been designed using the optimized lattice parameter and atomic position of ML CN with vdW correction, as seen in Fig. 5.1. Nine bilayer configurations (S_0–S_8) having energy differences and visible structural similarities are considered which are grouped into three sets: Set-1, which consists of S_3, S_4, and S_6, and Set-2, which consists of S_1 and S_2. Each set has nearly similar structures and cohesive energies, while all other dissimilar structures, such as S_0, S_5, S_7, and S_8, can be combined with Set-3. Even though thousands of random configurations of CN layers were initially taken into consideration, as also reported by Wang et al.[128] and Zuluaga et al.[130] with experimental verification and suggesting that variation in stacking configuration is dependent on synthesis temperature, this classification reveals the existence of only a few stable structural orientations.

The previous section covered how the initial models were designed in two categories: layers that were displaced over one another without rotation and an upper layer that had 180° rotations with displacement. Based on atomic alignment, all optimized structures can be further classified into two categories: planar (where there is no distortion in the z-axis for the bilayer) S_0, S_5, S_7, S_8 and corrugated (where there is distortion in the z-axis) S_1, S_2, S_3, S_4, S_6 geometry. This is because short-distance atomic orbital interaction causes these models to be designed. The final structures also show, as expected, the interlayer orbital interaction between C-N, C-C, and N-N with increasing levels of repulsion (decreasing strength of stability). The difference between the initial (3.275 Å) and final average atomic locations in the z-axis is used to determine the change in interlayer separation (ΔD), which is given in Table. 5.1, which shows the presence of triazine moiety of one layer over the void of another and comparable atoms (C-C, N-N) aligned over each other, clearly illustrates the importance of orbital interaction in the bilayer. The atomic configurations of Sets-1 and Set-2 are similar, which explains why the structures (S_0, S_5, S_7, and S_8) are not corrugated. On the other hand, atoms over the bonds (S_2, S_4) or non-similar (C-N) atoms (S_1, S_3, S_4, and S_6) exhibit atomic

alignment that results in corrugated geometry in the bilayer. Planar structures exhibit an increase in lattice parameters a and b, whereas corrugated structures show a decrease. The isolation of a layer in 2D and the suppression of interlayer interactions in c resulted in a negligible apparent change. Coulombs interaction because of the dominance of the s and p orbitals in planar structures in corrugated formations, the atoms' only visible changes are in the angle and bond length and the perpendicular p orbitals.

Each atom's charge density generates an equipotential surface surrounding the atoms in the multilayer structure of CN. When another layer is introduced near this surface, the atoms balance their forces according to the orbital interaction, resulting in structural changes. The region surrounding the atom encourages free movement of the atoms present in both layers, leading to an infinite number of possible positions and orientations; however, the number of possibilities decreases but stays high in the case of a multilayer system due to the constrained degree of freedom brought about by the presence of chemical bonds and LP. Similar structures in Sets 1 and 2 demonstrate this feature in our instance in terms of cohesive energy. The negative cohesive energy value, which can be found using Eq. 5.1, indicates that the reaction is exothermic, and Set-1, Set-2, and Set-3 are the most stable structures based on magnitude. According to the largest dissimilar atomic orbital interaction across all structures, $S_3/S_4/S_6$ type structures are the most stable in the bulk form of tri-s-triazine, according to comparable stability research. To further reduce its energy, a well-known design technique for the most stable bilayer—which involves eliminating N atom LP repulsion—needs to be remodeled to incorporate the greatest amount of interlayer C-N atomic orbital overlaps. In a multilayered system, layers glide over one another along the x-y plane as a result of the interlayer orbital coupling, resulting in the decrement of forces, and providing us with a few stable design options. The conjunction of planar electron distribution and interlayer orbital coupling will be most efficient in the bi-layer form of CN because, as previously reported, as the number of layers increases, the constraint increases and decreases the free movement of layers. Additionally, π-localization decreases along with the presence of reactive surface, preventing the

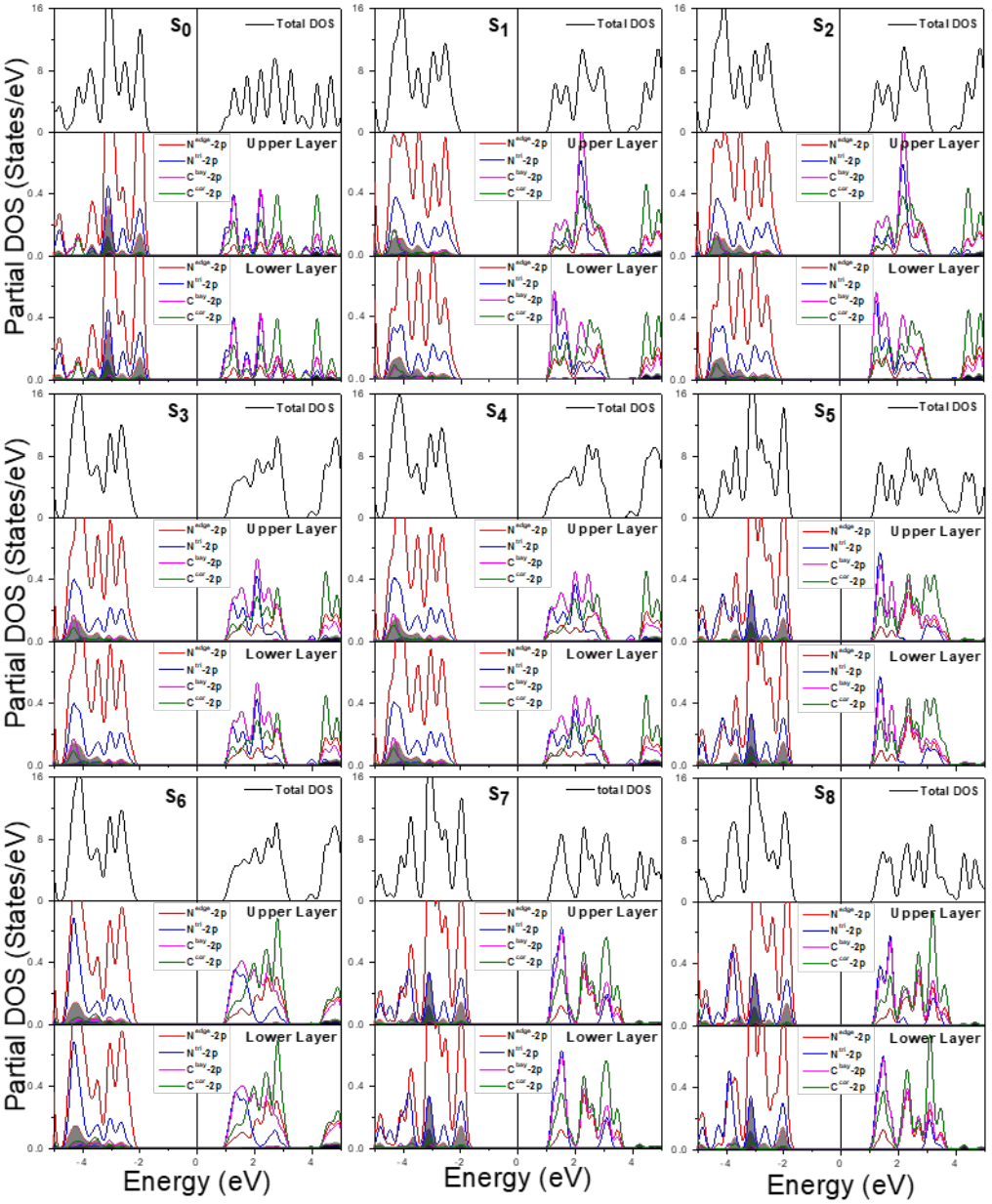

FIGURE 5.2: Illustration of total, partial DOS for $S_0 - S_8$ bilayer-CN configuration.

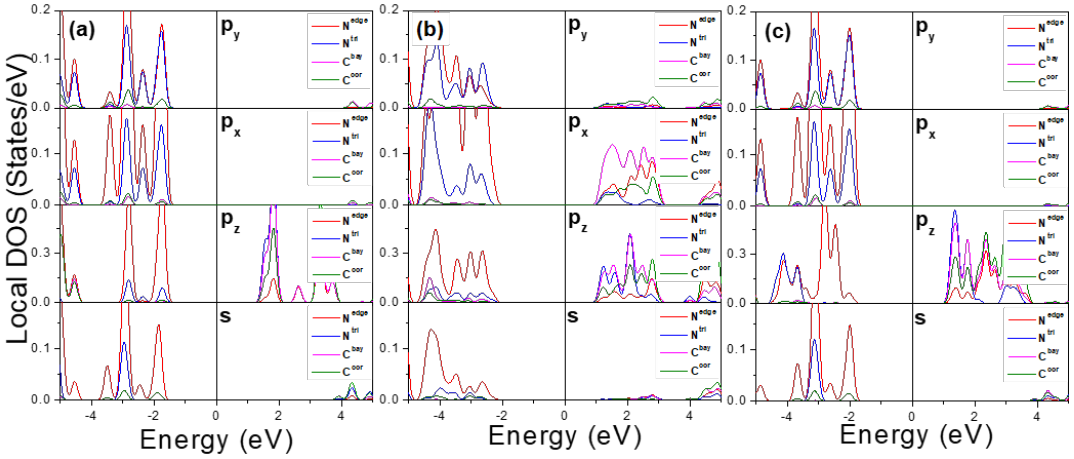

FIGURE 5.3: Orbital DOS for S_0, corrugated-S_3, and planar-S_5 bilayer geometry for CN.

system from traveling to global minima and rather confining itself in local minima to restrict structural changes.

The Table. 5.1 presents the calculated values of the band gap, related Φ, E_{BGC}, E_{vac}, and E_F of bilayers. Projected DOS (PDOS) that incorporates the individual orbital states has also been computed in addition to Total DOS, as seen in Fig. 3.3a for ML and Fig. 5.2 for BLs. We calculated band gap = 2.77 eV for ML, which was previously reported using PDOS. This indicates that N^{edge} plays a dominant role in bonding and hybridization of N^{tri} & C^{bay}, C^{cor} in the CB. The π-localization over the plane for rapid charge carrier mobility, the sp^2 bonding of the C-N atom, and the presence of LP at the N^{edge} atom are intrinsic characteristics of the ML. These features make them the most electronegative and, henceforth, a suitable site for intermediate adsorption for redox reactions, The ELF and DOS plots, shown in Figs. 5.4, 5.2, can be used to verify the structural changes in the BLs. The consistency in charge density adjacent to the plane in planar S_5 BL implies a balanced interlayer orbital interaction through the uniform distribution of spreading of charge cloud in the x-y plane, whereas the side glance of ELF shows a spherical charge distribution, which was ellipsoid for ML (Fig. 5.4). Corrugated structures show the repellent properties of the charge clouds and favorable arrangement between orbitals of C-N atoms across the z-axis of BLs. Figure 5.2 illustrates how

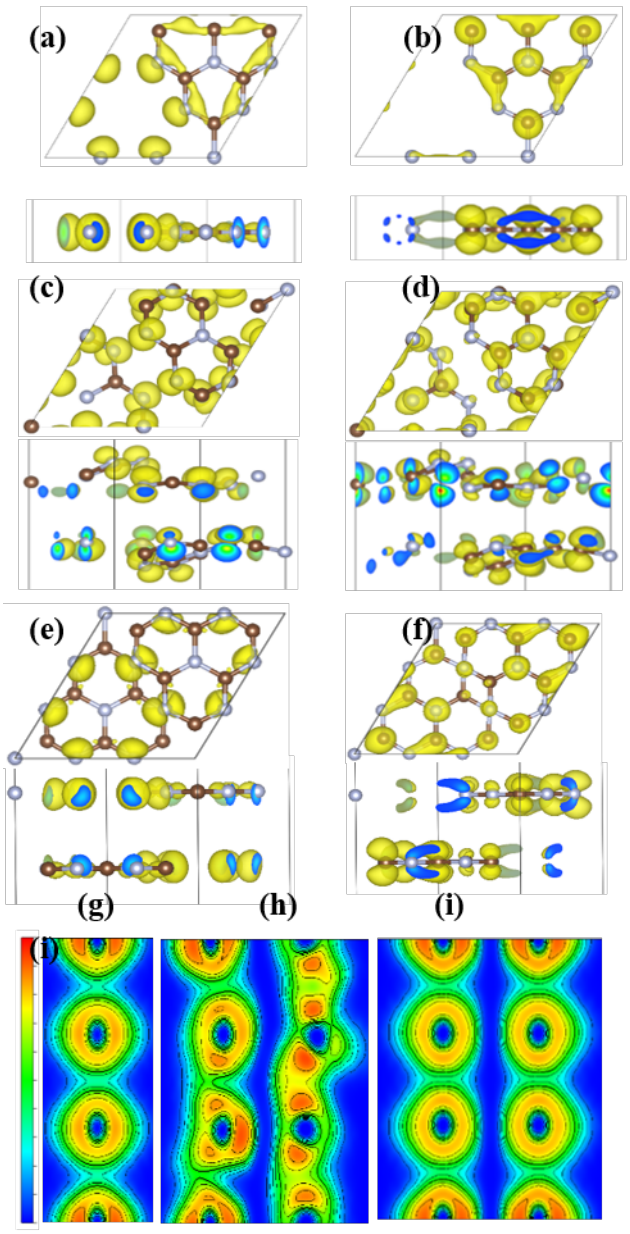

FIGURE 5.4: (a, c, e) Highest occupied molecular orbital (HOMO), (b, d, f) Lowest unoccupied molecular orbital (LUMO) top and side view and (g, h, i) 2D ELF contour (1 0 0 slab) for ML, S_3 and S_5, respectively

band gap decreases for planar BLs concerning (a) the distinct and sharp peak formed in the VBM region around -2.0 eV due to N^{edge} atom, (b) the pronounced peaks in the CBM controlled by N^{tri}/C^{bay} atoms in the region around 1.5 eV which migrate towards E_F, and (c) electronic states formed by s orbital for C/N atom migrate towards lower energy region, suggesting electron density confinement but slight delocalization in VB(CB) around -2.5 eV(2.0 eV) as compared to ML. On the one hand, because of its structural familiarity, the structure of Set-2 displays

almost the same properties for corrugated BLs (S_1, S_2, S_3, S_4, and S_8). However, as Table. 5.1 mentions, that a change in ΔD of triazine moieties in the bilayer causes a large change in the CBM. This change is also evident in the superiority of N^{tri} 2p-states in S_6 w.r.t S_3/S_4 in the CBM and C^{cor} around 2.75 eV, which is apparent from Fig. 5.2. On the other hand, we observe a slight difference in VB for Set-1 and a large change in the CBM. For BLs with 180° rotations (S_3, S_4, S_5, S_6, and S_7), the PDOS of both layers is the same; in the upper layer of the Set-2 structure, C^{bay} dominates the CBM, and lower layers exhibit hybridization of C^{bay} and N^{tri}. In contrast, BLs with 0°-layer rotation (S_0, S_1, S_2, and S_8) exhibit change in the PDOS of upper and lower layers, except for S_0.

TABLE 5.1: The calculated for cohesive energy (E_{coh}), interlayer distance difference (ΔD), band gap (E_g) , Fermi energy (E_F), vacuum energy (E_{vac}), work function (Φ), band gap center (E_{BGC}), effective mass of holes ($m_h^*(m_0)$), electrons ($m_e^*(m_0)$), effective mass ratio (β) and integrated absorption (α).

BL	E_{Coh}	ΔD	band gap	E_F	E_{vac}	Φ	E_{BGC}	$m_h^*(m_0)$	$m_e^*(m_0)$	β	$\alpha \times 10^5$
S_0	-0.02	-0.23	2.41	-4.31	3.15	7.46	-4.76	0.354	0.173	0.49	2.92
S_1	-0.11	-0.57	2.95	-4.56	3.47	8.03	-5.06	0.128	0.062	0.48	3.77
S_2	-0.11	-0.57	2.96	-4.55	3.47	8.02	-5.05	0.127	0.060	0.47	3.68
S_3	-0.13	-0.39	2.98	-4.52	3.48	8.00	-5.09	0.134	0.058	0.43	4.12
S_4	-0.13	-0.35	2.96	-4.51	3.48	7.99	-5.14	0.135	0.074	0.55	3.85
S_5	-0.05	0.01	2.68	-4.29	3.14	7.43	-4.62	0.352	0.478	1.36	2.89
S_6	-0.13	-0.34	2.97	-4.51	3.47	7.98	-5.12	0.139	0.080	0.58	3.93
S_7	-0.02	-0.04	2.61	-4.33	3.15	7.48	-4.65	0.344	0.156	0.45	3.39
S_8	-0.05	0.10	2.57	-4.32	3.14	7.46	-4.59	0.389	0.174	0.45	3.45

The band gap widens due to quantum confinement effects as one approaches ML; hence, BL should have a decreased band gap value to ML. However, the corrugated BLs in this work exhibit an increase in band gap, suggesting that orbital contribution is involved in the system. Fig. 5.3 presents the local density of states (LDOS) for ML & BL (S_3 & S_5; as typical structures from the corrugated & planar class. Figure 5.3(a, c) illustrates how N s, p_x, and p_y states dominate VBM, whereas C p_z states constitute CBM. Their planar shape is confirmed by sharp peaks in the VB region about -1.9 eV for ML and S_5 for N s, p_x, and p_y. The LDOS of S_3 reveals a minimal contribution from anti-bonding states of C s and p_y in CBM arising from the delocalization of empty states over the plane, a

substantial contribution from the N p_x orbital, and suppression of the existing C p_z states. According to Fig. 5.3(a and b), which compares the dominance of p_x states for N^{edge}, quenching of the p_y states for N^{edge} along with the merging and shifting of the 2p and 2s orbitals towards the lower energy in VB results in an increased band gap value. This indicates the role of orbital interplay over the quantum confinement phenomenon for stronger stacking configuration systems, conclusively supporting the experimental values.

To provide charge transfer and hybridization statutes, the HOMO and LUMO provide information about the potential existence of charge carriers in the atomic orbitals. As for ML, the localization of HOMO over low coordinated N atom from Fig. 5.4(a, b), while LUMO over C^{bay}, C^{cor}, and N^{tri} atom (also confirmed by PDOS) not only demonstrates uniformity in the z-axis but also decreases the separation of $e^- - h^+$ pair and eliminates the material's photocatalytic efficiency. Consequently, to increase efficiency, we need to induce the smaller binding strength by increasing occupancy in the anti-bonding orbital. The bilayer's corrugation for S_3 causes an increase in the difference of e^- to N in its π^* anti-bonding orbitals from the LP states of bonding orbital, and an increase in the unoccupied states of C in CB as a result of π-conjugation. These findings, taken together with Fig. 5.4(c, d), indicate the direction of electron delivery towards the most favorable site for the redox reaction intermediate adsorption. As a result of interlayer interaction, Fig. 5.4(e, f) show uniform localization of charge density over the atoms in both HOMO and LUMO. The HOMO exhibits LP bending due to the presence of void, while the vanishing of charge density in LUMO as compared to ML indicates its decreased π-conjugation, resulting in reduced surface site for reaction. For ML, Fig. 5.4g shows the equipotential surface from the ELF contour of the (100) plane. Regarding Fig. 5.4h, the system's stability is attributed to the promotion of partial hybridization in the S_3 bilayer between π-LP after the downward shift of LP. This is because the higher charge density and tilt angularity of both layers compensate for the on-site orbital resonance, this is not seen in S_5 (Fig. 5.4i). Although it provides reactive sites on each side of the system for simultaneous reduction-oxidation reaction in the bilayer (S_3)

configuration.

The photocatalytic activity of a material is determined by its charge carrier mobility and recombination rate, in addition to the presence of a band gap in the visible spectrum. Reduced effective mass ($m^* = e\tau/\mu$, where e is the electronic charge, m^* is the effective mass, τ is the collision time, and μ is the carrier mobility) results in higher charge carrier mobility, which not only shortens the duration of photo-induced $e^- - h^+$ pair transport within the material but also accelerates charge displacement over the surface to prevent charge accumulation and provide a clean surface for enhanced redox activity. Values of m_e^* and m_h^* are given in Table. 5.1, and the effective mass ratio ($\beta = m_e^*/m_h^*$). For $e^- - h^+$ pairs, β also correlates to the variance in the effective mass; a lower variance value denotes slow activity but quick recombination, and vice versa. For S_5 and S_8, respectively, Γ-point of CBM and M-point of VBM is used to compute m_e^* and m_h^*, whereas for ML and the remaining BLs, Γ-point of CBM and K-point of VBM are used. The m_e^* and m_h^* values for ML, S_0, S_5, S_7, and S_8 (planar) exhibit higher effective mass due to small band curvature, which results in low electron mobility and heavy holes leading to low activity. On the other hand, the comparative lower effective masses for S_1, S_2, S_3, S_4, and S_6 (corrugated) point toward high photo-induced charge carrier mobility, implying its significance in enhancing the photocatalytic activity. From Table. 5.1, the highest mobility of $e^- - h^+$ pair is observed for S_3. With $m_e^* > m_h^*$, S_5 is an exception because of the modest variance and tiny curvature of VBM in comparison to CBM. In contrast, S_2, S_3, S_7, and S_8 exhibit more variance than ML, which puts them one step closer to improved photocatalytic activity. Fig. 5.3 illustrates this behavior for the CB as a result of p_x/p_y orbital activation; however, despite the complementary features of interlayer orbital interaction and π-conjugation (S_1, S_2, S_3, S_4, and S_6), the curvature of the VB and hence the mobility of holes increased due to HOMO hybridization. Thus, issues with electron-hole pair recovery time are eliminated by raising photo-generated charge carrier mobility, their effective separation, and a decreased recombination rate. Thus, in the search for an effective photocatalyst,

S_3 declares its supremacy in charge separation among all structures as a result of low recombination rate and high electron mobility.

5.4 BL-CN Optical and Photocatalytic Analysis

The position of band edges related to the reduction-oxidation potential, the existence of its forbidden energy area in the visible spectrum, and the increased mobility of the $e^- - h^+$ pair with a lower rate of recombination determine the overall amount of water splitting by any photocatalyst. To modify the scale to a NHE; (E(H^+/H_2) = 0 V versus NHE) as shown in Fig. 5.5a, we calculated band edges from VBM and CBM of DOS with a correction of E(O_2/H_2O) = -4.44 eV (reduction potential) for the investigation of photocatalytic activity. Band edges for all the BLs indicate their potential use in overall water splitting, though nearly equal amounts of potential straddle the water's redox level for S_1, S_2, S_3, S_4, and S_6. These structures benefit from lower E_F values than ML, S_0, S_5, S_7, and S_8, which increases the probability of easily crossing the prohibitive overpotential of 1.56 eV for ML CN measured by Wirth et al.[82] The S_3 configuration is found to be the most suitable based on stability, band gap, charge separation, rate of recombination of charge carriers, absorption in the visible region, and band edges. With this bilayer arrangement, we will continue to study the thermodynamics of the OER/HER. For the study of optical properties using HSE06, the imaginary part ($\epsilon_2(\omega)$) and frequency-dependent absorption coefficient ($\alpha(\omega)$) of the complex dielectric function are computed and presented for ML, S_3, and S_5 in Fig. 5.5(b, c), and the insets show corresponding data using PBE functional. The redshift of $\alpha(\omega)$ for BLs vs ML (Black color) in Fig. 5.5b suggests a rise in absorption in the visible range (shaded yellow region), which is further supported by the integrated absorption values are tabulated. For BLs, is shown in Table. 5.1, while for ML, it is 2.01×10^5. Because of the activation of a prohibited dipole transition channel in ML produced from interlayer orbital interaction, this points us in the direction of employing BLs to increase visible light absorption resulting in higher

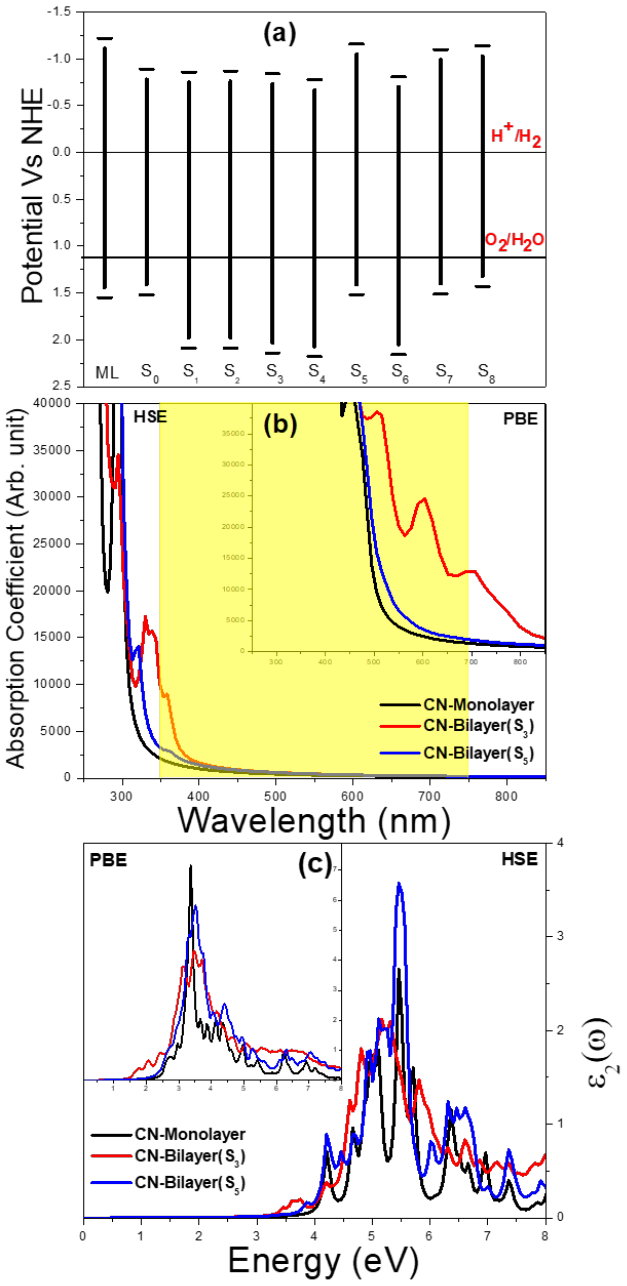

FIGURE 5.5: (a) Band edges for ML, S_0-S_8 CN configuration, (b) absorbance, and (c) imaginary part of dielectric function for ML, S_5, S_3 geometry for HSE functional. Inset represents $\alpha(\omega)$ and $\epsilon_2(\omega)$ for PBE functional.

photo-generated charge carriers for high photocatalytic activity. However, a large peak located at 325 nm along the x-axis for the former design is the result of a significant positive difference between the absorption value of the corrugated and planar structures.

According to Fig. 5.5c, the peak at 5.5 eV for ML CN corresponds to the elec-

tronic transition from the top of VB, which is dominated by occupied N^{edge}-2p states, to the bottom of CB, which is made up of unoccupied hybrid states of N^{tri}, C^{bay} atoms. Due to the permitted transition from VBM to CBM in S_3 and S_5, which is prohibited in ML, the low energy peak in the imaginary function of dielectric in these two sets of data also explains the larger absorption in comparison to ML. The analysis concludes that interlayer orbital coupling plays a role in expanding the band gap and absorption in the visible region, and that corrugation causes π-delocalization, which further enhances the optical property due to synergistic effects. Among all the structural configurations, S_3 is determined to be the most optimal.

5.5 BL-CN Reduction-Oxidation Mechanism

5.5.1 Oxygen Evolution Reaction

The overall study of water splitting requires crossing band edges across redox levels in addition to overpotential values inside the band edges; the greater the OER/HER activity, the narrower the overpotential ($\eta^{OER/HER}$). We employ the four electron reaction pathways that Nørskov and colleagues [74, 75] devised to compute and investigate the impact of overpotential for effective OER activity. The crucial stage in OER is the adsorption of the H_2O molecule over the substrate, which is followed by the optimal *OH, *O, and *OOH intermediate. The relevant adsorption energy has been computed and is susceptible to energy and force minimization. We have taken into consideration six distinct reaction sites, as seen in Fig. 5.6(a, b), even though in-plane π-conjugation offers several adsorption sites on either layer based on electronegativity observed from the HOMO-LUMO and other work on diverse absorption sites over CN. Site-A, B, C, D, E, and F correspond to positions above the void of UL, over the N^{tri} atom of LL, below the N^{edge} atom of LL, above the N^{edge} atom of UL (across Site-C), and below the corner carbon of LL and the bay carbon of LL, respectively.

The water molecule adsorbed at 3.42 Å above/below the corresponding layer

demonstrates alignment with the H atom aimed towards the N^{edge}, forming a hydrogen bond, except for H_2O adsorbed over Site-C, which drifts away. This alignment is caused by the molecule's polarity. Site-A, B, C, D, E, and F had absorption energies (ΔE_{H_2O}) of -0.29, -0.16, 0.04, -0.16, -0.35 and 0.038 eV, respectively, indicating physisorption, with Site-C being the least favored site. Strong adsorption causing feasibility in subsequent reaction stages is indicated by a larger energy value of ΔE_{H_2O} than ML because of interlayer interactions. The conversion of H_2O into *OH by releasing a single $e^- + H^+$ pair is the first step in OER. In this instance, *OH adsorbed and formed a single bond on the substrate's surface by chemisorption. The C^{bay} atom of the corresponding layer forms bonds with the O atom in Sites A, B, C, and F, whereas the N^{edge} atom forms bonds with Site-D, and no bonds form with Site-E. As a consequence, the values of ΔE_{*OH} are 2.21, 2.03, 2.07, 2.05, 2.60, and 3.08 eV. Site-B has the lowest computed value of ΔG_1 for the first step (*OH), suggesting high *OH adsorption. In the second step, the $e^- + H^+$ pair is removed further, leaving isolated O*, which retains its bonds with the C^{bay} and N^{edge} atom for Sites-A, B, C, E, and D, F, respectively. Meanwhile, massive charge transfer for Site-D causes π-delocalization, elevating it higher on the stability scale for O* adsorption because of the bond formed with N^{edge} and quick distribution of charge over corrugated geometry. The third reaction step, which involves the addition of the H_2O molecule, transforms the H_2O + O* to OOH*+ ($e^- + H^+$) by forming a hydroxyl intermediate. Site-A exhibits complete molecule desorption, while Sites B, C, E, and F show a change in the orientation of the H atom bonded to O-O, and Site-D involves detachment of hydroxide due to strong covalent bonding of O-N.For Site-A, B, C, D, E, and F, ΔE_{OOH*} is 5.43, 5.85, 5.84, 6.12, 5.93, and 5.83 eV, following the amount of electron transfer with free energy (ΔG_3). To retain $\Delta G_{1-4} = 4.92$ eV, the last step entails the creation of an oxygen molecule together with a $e^- + H^+$ pair, whose free energy is determined by the appropriate equation. All four sites have an uphill free energy value at U = 0.0 eV. For Sites A, B, C, E, and F, the first and third steps, respectively, displayed the maximum free energy change value, establishing those reactions as

limiting steps and the corresponding values to be used for the overpotential calculation. This is illustrated by the free energy profile for various intermediates adsorbed at each site, which is plotted in Fig. 5.6(c-h), in which the reaction coordinates on the x-axis translate to the step number. In addition to the free energy profile at U = 0.0 e V, we have calculated ΔG at equilibrium potential (U = 1.23 V) and at U = η^{OER} + 1.23 V. The results show that $\eta^{OER}_{BL} < \eta^{OER}_{ML}$ and that all four of the reactions at U = η^{OER} + 1.23 V are exothermic, suggesting that the reactions can potentially carry over. According to the study, the OER activity of sites A, B, and C is enhanced by $\eta^{OER} < 1.56$ V (prohibitive overpotential) and $\eta^{OER} < |E_{VB}|$. On the other hand, Site-B is the most suited surface reaction site since it has the lowest value of $\Delta G_1 = 2.38$ eV, which implies $\eta^{OER} = 1.15$ V.

5.5.2 Hydrogen Evolution Reaction

Eqs 5.2, 5.3, are used to illustrate the Volmer-Heyrovsky pathway for HER, where the crucial component of the HER activity determined by Eq. 5.4, is the intermediate state's Gibbs free energy, or $|\Delta G_{*H}|$ or $|\Delta G_{H_3O*}|$.The formulation of Nørskov et al. [73–75] for each adsorbate, and its counterpart shows that, while the negative value indicates the preferred adsorption site, its optimum value is zero. The H atom chemically bonds to the N^{edge} of each layer at Site-A, C, D, and E with ΔE_{*H} values of -0.44, -0.58, -0.51 and -0.53 eV, respectively showing $|\Delta G_{*H}| < 0.35$ eV it indicates weak H atom adsorption across BL and is half the value of ML, indicating weak adsorption of the H atom over BL. These adsorption sites are consistent with our simulation of adsorption sites as examined in the OER study. Nevertheless, due to the confinement of the H atom over the 3-fold coordinated N (N^{tri}) atom and the creation of an H-C bond, Sites B and F exhibit $|\Delta G_{*H}| > 3.0$ and 1.2 eV, ruling out this scenario. The $|\Delta G_{*H}|$ vs. Reaction states are displayed in Fig. 5.6i, where Site-A is determined to be the most suited location, here Pt is considered as a reference. Due to the distinct BL configuration with C-N orbital overlap, which creates an excess charge at the reaction site as opposed to the BL

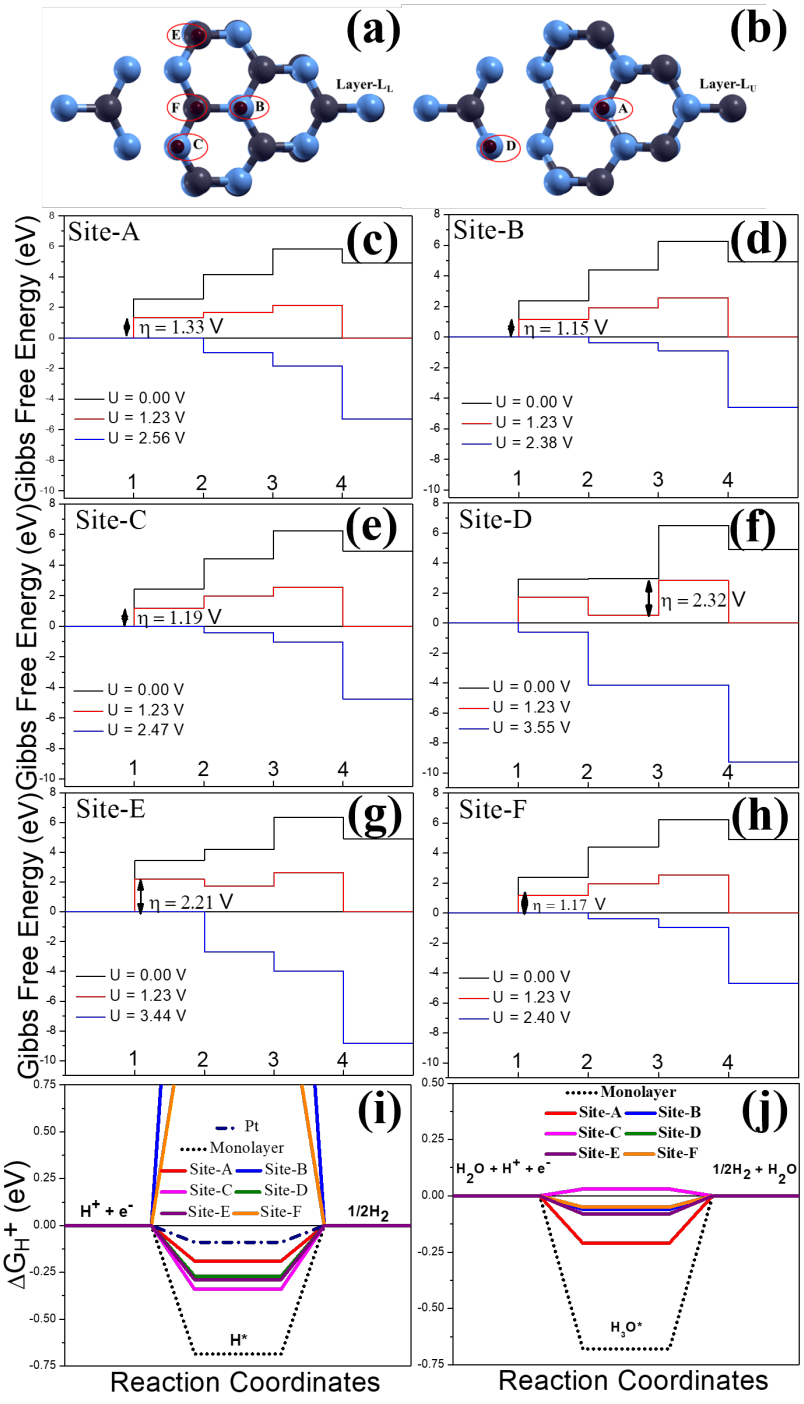

FIGURE 5.6: (a, b) Sites over the upper/lower face of S_3, (c-h) Gibbs free energy for OER, (i, j) for HER over respective sites. HER includes ML and Pt for reference.

with N-N orbital interaction (i.e S_5), the overpotential measurement for site A (-0.20 V) is smaller than the value earlier reported by Niu et al. [131] The H atom separated to produce *H + H_2O as a result of the adsorption of H_3O* over the same sites. All of the sites exhibit *H chemisorption to the corresponding layer's 2-fold coordinated N atom, and the H_2O molecule drifts away to establish an H-bond with another N^{edge}. Site-C is energetically most favorable, but Site-D will be preferred over C because it lies on the negative side, as shown from Fig. 5.6j with an overpotential value of -0.05 V. The presence of an additional H_2O molecule-assisted chemisorption of confined H atom over N^{tri} for Site-B, along with a decrease in the value of $|\Delta G_{*H_3O}|$ for Site-B, C, and D, but an increase for Site-A.

5.6 BL-CN Interlayer-Intralayer Charge Dynamics

Here, the charge transfer investigated within the interface and on its surface has been divided into two categories: interlayer charge redistribution and π-delocalization. It is observed that in the case of OER/HER, interlayer charge transfer is minimal in the absence of intermediate species. This is changed upon the adsorption of the intermediate by altering the π-delocalization of orbitals and interlayer interaction, which in turn influences the reaction's free energy value. In the case of HER, the sites with the highest order of π-delocalization and interlayer charge redistribution, namely Site-A (H-atom) and Site-C (extra H_2O molecule), are shown to have the lowest adsorption energy. The order of interlayer charge migration and π-delocalization is determined to be lowest among other investigated sites for the rate-determining step (with *OH adsorption) in the case of OER for the best appropriate site (Site-B). While it is said that Site-A, D/F, and B are the best sites for the HER (H, H_3O) and OER, respectively, other sites have lower overpotential values than ML CN. By establishing a new charge transfer pathway that was not present in the ML, the synergistic effect of inter and intralayer charge conjugation increases the surface reaction sites.

This combined effect has been confirmed by HOMO-LUMO and LDOS through the activation of the p_x and p_y orbitals in the corrugated configuration and the hybridization of the p_z orbital, where S_3 has proven its suitability in terms of the largest effective mass variance and optical absorption in the visible region, thereby lowering the overpotential in comparison to the ML and boosting photocatalytic efficiency.

The activation of orbitals for the interlayer charge transfer within the interface is a contactless electron transfer pathway. However, the activation of the forbidden transitions has increased the optical absorbance but the lack of contact between the layers for efficient and directional charge transfer through bridging the layers has limited the utilization of the bilayer for simultaneous HER and OER. To overcome this shortcoming of unidirectional charge transfer, enhance the synergistic water splitting into H_2, O_2, and open the gates of the interplay of $\vec{E_{if}}$ and $\vec{E_{il}}$ generation, we have explored the Li intercalated BL-CN.

5.7 The Case of Lithium Intercalated g-C_3N_4

By creating and enhancing the vdW connection between chemically inert layers of the photocatalyst [135], one can encourage the migration of photo-generated charge carriers and lower the rate of recombination. For effective photocatalyst design, strategies such as bilayer formation incorporating interlayer orbital overlap [9], intercalation of alkali/alkaline earth metals for directional charge delivery, and heterostructure production utilizing the S/Z electron transfer scheme [136] have been implemented [137, 138]. Numerous functionalization approaches have been used to accomplish charge separation, mobility increase, longer lifetimes for photogenerated charge carriers, and lower recombination rates. Through the intercalation/decoration of Cs, Rb, K [28, 29], K/O [139], Ca [140], Ba [141], and Sr [142], Dong's group has exclusively increased the efficiency of CN for NO removal. This process is controlled by vertical electron transfer, which is established

by extending $\pi-$ conjugation, localizing electrons around a metal atom, activating reactants, and resulting reactive oxygen species. Conversely, Na has reduced catalytic activity and a shorter lifespan of charge carriers as a result of a higher electron concentration in the planar area [143].

Li [137, 144, 145], Li/Na/K [146], and Li/Cl [147] demonstrate notable improvement in photocatalytic N_2 fixation, dye degradation, and H_2 generation in the $(BL-CN)$ assembly, both experimentally and conceptually, suggesting that they may be the atom or atoms capable of bridging stacked layers [146, 147]. Due to its small ionic radii, Li can interconnect stacked layers without changing the CN ring form. Reduced band gap, VB shifting, and different interlayer spacing for co-intercalation, which promotes electron migration across the layers, are factors contributing to the enhanced catalytic activity of CN. Li's involvement in lowering the Φ of CN or enhancing electron affinity is projected by substitutional doping [148, 149] and adsorption of Li [27, 101] over the triazine moiety, while Li-N interaction controls the electron transfer channel for adsorbent activation. Potential photocatalytic suitability of Li linked CN is demonstrated by improved optical absorbance and redshift, which are complemented by charge transportation and separation capabilities related to Li's drive to release its outer electron. $\vec{E_{il}}$ induced by the potential gradient between stacked layers in K, Rb, and Cs bridged CN guides electron migration vertically [28, 29]; this is comparable to the $\vec{E_{il}}$ set across heterostructures owing to the difference in Φ [89, 136]. The charge dynamics within the photocatalyst are controlled by $\vec{E_{il}}$ across the semiconductor-metal and semiconductor-semiconductor junctions in addition to band edge alignment. Moreover, co-doping of S/K- [104], halogen atoms/K- [40], B/K-, and Zn/K [41, 103] inside CN has demonstrated increased H_2 evolution and CO/CH_4 synthesis, balancing the interlayer and intralayer electron distribution. When "surface decoration" and "intercalation" were combined to form an internal vdW heterostructure (IvdWH), it was demonstrated that O incorporation in the K-functionalized CN [139] enhanced the charge transfer channel by strengthening the internal vdW interaction and localizing electrons around O, which resulted in the spatial separation of photoinduced charge carriers. On the other hand, the

chemical kinetics of any reaction that occurs at the photocatalyst surface are controlled by the combined action of the $\vec{E_{if}}$ that forms at the reactant-photocatalyst interface and the polarizability of interacting molecules [150–152]. The charge migration within the $TpPa-1-COF/CN$ [153] structure is governed by the formation of an electric field at the $\pi-\pi$ conjugated hetero-interface [154].
We have studied the independent OER and HER over Li intercalated CN bilayer (Li-CN), along with electronic and optical properties using DFT, to understand IvdWH formed by the adsorption of various intermediates adsorbed during the reaction. We have done this by using a traditional computational hydrogen electrode (CHE) method [73, 75]. The addition of Li-atom to the CN network has been shown to boost certain photocatalytic activity; nevertheless, its water-splitting potential has not yet been explored. A thorough theoretical analysis of Li-intercalation's function in CN for OER and HER will confirm its eligibility for photocatalytic activity and provide more insight into the current experimental findings. Additionally, we have computed concurrent OER and HER in the event of the presence of two water molecules on the surface of Li-CN. This allows us to better understand the interaction and mutual dependence of $\vec{E_{il}}$ and $\vec{E_{if}}$, an important topic that has not been thoroughly studied since the introduction of homo- and hetero-layered structures. A step-by-step charge analysis is used to unravel and address the charge transfer mechanism governed by $\vec{E_{il}}/\vec{E_{if}}$ formation in Li-CN. This charge transfer mechanism is then verified by studying the activation barrier (E_a), which is calculated using the NEB approach [4, 5].

5.8 Li-CN Computational Models and Details

For structural relaxation and computation of HER and OER reaction studies of Li-CN, a *ab-initio* based DFT calculations [49, 55, 56] with in-built Kohn Sham formulation for plane wave-based method as implemented in the Quantum Espresso Package [76] is examined. A kinetic energy cut-off of 60 Ry is employed in the computation, in addition to an ONCV [113] for core correction. vdW interaction is described using Grimme-D2 dispersion correction. A 20 Å vacuum

space is taken into consideration to prevent periodic inter-slab contact along the z-direction as well. To maintain the computational parameter close to our previous work, the Coulomb interaction in the z-direction was truncated. With an electronic convergence threshold of $10^{-6} a.u.$, all the structures are relaxed. Per atom, maximum force less than 10^{-3} $a.u./$ Å. With a k point grid of $5 \times 5 \times 2$, is taken into consideration for atomic position relaxation using the PBE-GGA [58]. A self-consistent field cycle is used to compute electronic parameters such as DOS (DOS), Löwdin charges, and EPP. In addition to GGA, the Wannier90 package's hybrid functional HSE06 [60, 61] is taken into consideration for precise band gap calculation at $3\times3\times3$ k-point mesh. This is followed by the band structure computation process, which uses MLWF [68, 69, 155].

FP-LAPW method as implemented in Wien2k code [59] has also been used to carry out the electronic and optical properties such as band structure, absorption coefficient ($\alpha(\omega)$), and the imaginary part of dielectric function ($\epsilon_2(\omega)$), DOS, partial DOS (PDOS), local DOS (LDOS), for BL-CN and Li-CN. TB-mBJ (Tran-Blaha modified Becke-Johnson) [67] potential has been applied to provide a more accurate estimate of the electronic bandgap and optical characteristics. The muffin-tin radii for Li, C, and N atoms in Li-CN are 1.18, 1.25, and 1.75 a.u., respectively, to yield smooth fluctuation at the boundaries indicated by these radii between the interstitial-APW and the core spherical harmonics. The muffin-tin radii for the N and C atoms in BL-CN are 1.29 and 1.22 a.u., respectively. The value of $R_{mt}K_{max}$ was set at 7.0. Here, R_{mt} is the minimum muffin-tin radius value, and K_{max} is the greatest K for the plane waves utilized in the computations. The expansion of the wavefunctions was done using the maximum value of angular momentum, $l_{max} = 10$, whilst the Fourier expansion (G_{max}) is maintained at 12. All computations were done on a k-mesh grid of $3 \times 3 \times 1$.

TABLE 5.2: Charge difference for *BL-CN* [9] and *Li-CN* between the upper & and lower layers.

	BL-CN	*Li-CN*
$\|\Delta Q_{LL}\|$	0.8902	0.4922
$\|\Delta Q_{UL}\|$	0.8905	0.3614
$\|\Delta Q_{il}\|$	0.0003	0.131
$\|\Delta Q_{p_z}\|$	0.0008	0.115
$\|\Delta Q_{p_x}\|$	0.0006	0.035
$\|\Delta Q_{p_y}\|$	0.0008	0.064

5.8.1 Water Splitting Redox Kinetics

The 29-atom *Li-CN* system is studied for OER and HER using both traditional [73–75] and simultaneous methods (involving two water molecules). For OER, the corresponding intermediates were adsorbed and relaxed sequentially, whereas for HER, single-atom/molecule optimization is needed. Two H_2O molecules had been released for both simultaneous OER and HER as they are sufficient for complete parallel OER & HER with $\sim 4\times 10^{14}$ H_2O / cm^2 interaction with the surface. The CI-NEB [4, 5] approach was also used to examine the reaction kinetics and to compute the activation barrier for each phase of simultaneous OER & HER. The starting and final structures in the CI-NEB computations were optimized structures derived from DFT. With 12 pictures for each of the four phases, CI-NEB computations converged at a path threshold of 0.05 eV Å$^{\check{}1}$.

TABLE 5.3: The ΔQ_{il} interlayer charge difference and the adsorption energy for the reaction intermediates of OER and HER for the *Li-CN* system.

Li-CN	H_2O		OH		O		OOH		H		H_3O	
	$\|\Delta Q_{il}\|$	E_{ads}	$\|\Delta Q_{il}\|$	E_{ads}	$\|\Delta Q_{il}\|$	E_{ads}	$\|\Delta Q_{il}\|$	E_{ads}	$\|\Delta Q_{il}\|$	E_{ads}	$\|\Delta Q_{il}\|$	E_{ads}
Site-1	0.439	-1.013	0.615	-0.054	0.262	2.069	0.535	3.052	0.956	-0.795	0.649	-0.552
Site-2	0.649	-0.546	0.573	0.598	0.838	2.689	0.579	4.569	0.989	-0.735	0.270	-1.076
Site-3	0.362	-0.789	0.623	-0.066	0.332	2.222	0.519	3.122	1.036	-0.730	0.277	-1.117
Site-4	0.462	-1.009	0.622	-0.055	0.272	2.068	0.545	3.045	0.958	-0.798	0.319	-1.251
Site-5	0.670	-0.521	0.647	-0.142	0.334	2.300	0.584	3.574	0.969	-0.798	0.337	-0.701
Site-6	0.659	-0.597	0.378	0.619	0.353	2.146	0.583	3.381	0.979	-1.043	0.442	-0.397

To understand each reaction step and the charge transfer mechanism, from the calculated Löwdin charges, interlayer (ΔQ_{il}) and interfacial (ΔQ_{if}) charge difference

is calculated using the following formulas:

$$\Delta Q_{il} = Q_{LL}^{system} - Q_{UL}^{system} \tag{5.5}$$

$$\Delta Q_{if} = Q_{adsorbate}^{system} - Q_{adsorbate}^{VEC}, \tag{5.6}$$

Here, UL: Upper layer; LL: Lower layer; VEC: Valence electron count;
Apart from the calculation of ΔQ_{il}, and ΔQ_{if}, we have calculated the difference in the charges ($\Delta Q_{UL/LL} = Q_{UL/LL}^{system}$ - $Q_{UL/LL}^{VEC}$) within the interlayer to simply the charge transfer mechanism. For a simplified understanding following points are highlighted:

1. Given that VEC is constant ($Q_{LL/UL}^{VEC} = 64$), ΔQ will decrease as the system's total charge increases.

2. For instance, we compute $|\Delta Q_{UL/LL}^{Li-CN}|$ of 0.4922/0.3614 e^- and $|\Delta Q_{UL/LL}^{Li-CN-H_2O}|$ of 0.792/0.1163 e^- for $Q_{UL/LL}^{Li-CN}$ of 63.5078/63.6386 e^- and $Q_{UL/LL}^{Li-CN-H_2O}$ of 63.208/63.8837 e^-, respectively (Table. 5.2).

3. $\Delta Q^{Li-CN/Li-CN-H_2O}$ computations do not take the charge of the Li atom or the H_2O molecule into account.

4. When $Q^{Li-CN/Li-CN-H_2O}$ decreases (increases) on LL (UL), $\Delta Q^{Li-CN/Li-CN-H_2O}$ increases (decreases) on LL (UL) from pristine to H_2O adsorbed Li-CN (Table. 5.3)

Intermediate relaxation over the surface for the OER and HER have been performed in two ways (i) Traditionally Eq. 5.2, 5.3, have been considered, (ii) Simultaneous OER & HER over the surface includes the adsorption of two H_2O as an initial step following-

$$* + 2H_2O \rightarrow *OH + *H + H_2O \rightarrow *O + *H + *H + H_2O \tag{5.7}$$

$$\rightarrow *OOH + *H + H_2 \rightarrow * + O_2 + 2 \times H_2 \tag{5.8}$$

In this case, one of the two H_2O will start the dissociation process that will produce OER & HER and hydroxyl & hydrogen, respectively, while the other will contribute to the formation of a $\vec{E_{if}}$ reported as electric double layer [156] to influence the former H_2O and lead to charge conjugation over the surface. As the

catalyst surface interacts with the water layer, an electric field at the interface is formed, and this electric field helps to modify the reaction kinetics. The following stage leading to *O conversion will be started by this *OH by releasing H. Hydroxyl and hydrogen will bond to their respective sites for oxidation and reduction. This H can now produce H_2 either by the Tafel mechanism or the Heyrovsky process, in which case it will link to another electronegative site. The dissociation of H_2O will occur after the formation of *O, 2*H, and cyclically, the third H_2O will replace the second to preserve the $\vec{E_{if}}$. The dissociation of H_2O occurs because the third step yields H^+ & OH^-, where the hydroxyl leads to *OOH. The third H^+ can again form H_2 through Heyvrovsky or Tafel (if Heyvrovsky did not occur in the preceding step). Following a successful H_2 desorption, *OOH and *H remain on the surface, which prompts another H_2. O_2 desorption then completes the reaction. Simultaneous HER and OER simulation using two water molecules is done for three reasons: (i) to study the charge transfer throughout the reaction since, in contrast to conventional OER/HER, the number of atoms will remain constant; (ii) to comprehend the impact of surface terminations on the process and the corresponding reaction; and (iii) to study the impact of charge transfer between adsorbate and adsorbent and the role of H_2O in creating an electric field within the interface.

5.9 *Li-CN* Structural, Electronic and Optical Properties

The change in electronic characteristics is represented by structural variation; in this case, the original structure is further corrugated by Li intercalation in *BL-CN*. Fig. 5.8(a-b) illustrates this. As seen in Fig. 5.11a, the Li atom initially positioned at the center of *BL-CN* interacts with N^{edge} [9] atoms of the upper and lower layer (UL and LL) with bond lengths of 2.01, 2.28, 2.14, and 2.58 Å. This bilayer bridging not only increases the spatial displacement of layers across

the xy-plane but also decreases the average interlayer separation by 0.286 Å. The changed orbital interaction between the layers controls significant variation in the layer alignment caused by the Li-intercalation. Previous findings have demonstrated that the interaction of alkali metal with edge-N [139, 140, 142, 143] results in interlayer bridging of alkali metal intercalated CN. Li interacts with the N atom based on the edge-negative character, interlayer orbital interaction, and bending lone pair of the edge-N atom over/within interlayer tendencies. Atoms other than edge-N have a suppressed electronegative character relative to N_{edge}, which means that they do not tend to form a strong connection with an alkali element. The intralayer charge redistribution caused by the charge transfer from Li to $N_{UL/LL}$ results in corrugation, yet there is no distortion in the CN network/ring. As previously reported, the integrity of the CN tri-s-triazine structure is preserved experimentally, indicating that its synthesis is viable at the current concentration (3.57 at%) [147, 157].

An n-type extrinsic semiconductor with a partly filled CB has formed, as shown by the electronic characteristics of Li-CN from energy bands and DOS, as seen in Fig. 5.8c. The change in E_F from BL-CN to Li-CN is ascribed to the introduction of electrons from the Li-2s orbital into the system. This is a result of vertical interaction and causes a contribution in the frontier orbital (FO). In BL-CN, the UL/LL VB/CB states are comparable. Negligible interlayer charge transport is observed (see Table 5.2, Eq. 5.5). Figures show the plotted partial and local DOS (PDOS and LDOS). The contributions of the 2p-orbital of N_{UL} are highlighted in Fig. 5.8c and 5.7, respectively. Origin of N_{UL}^{bridge}, C_{UL}, N_{LL}, C_{LL} in CB, C_{LL}, N_{LL} in VB. The VB maxima have 2p orbitals, which indicate strong π-conjugation. Steep C_{UL} states and broad VB of Li are responsible for the relative flatness of partially occupied CB and the bending of VB maxima from $M \rightarrow K$, respectively. The computed band gaps are from $K \rightarrow K$ (band gap = 2.36 eV) and the indirect band gap from $K \rightarrow M$ (band gap = 2.34 eV). Comparable characteristics can be seen in the energy band (Fig. 5.7) that was computed using the Wannier function. Due to its sharp CB and VB on the scale of effective mass variance (β)

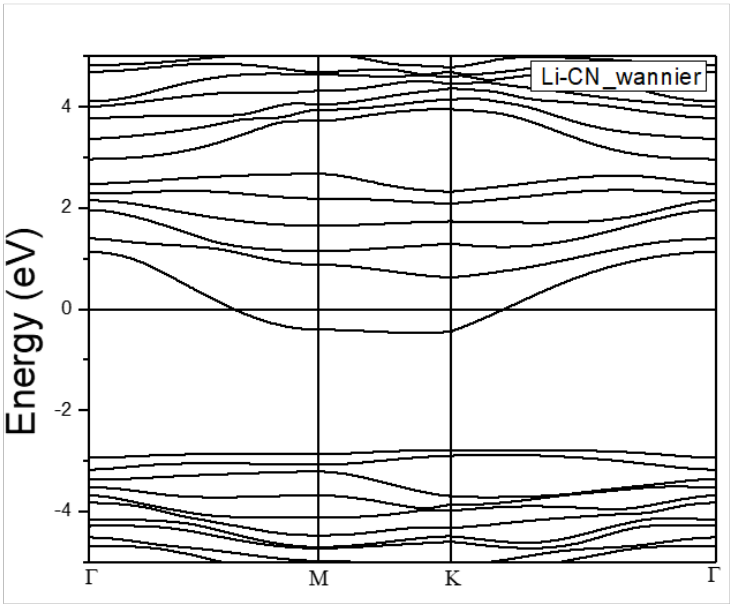

FIGURE 5.7: Band dispersion curve for *Li-CN* using Wannier functions that are maximally localized.

is the effective mass of electron/hole), highly curved CB minima attributed to significant electron mobility and low curvature of VB maxima owing to bulky holes in *Li-CN* challenge *BL-CN*, inferring $\sim$ 2.2 times a reduction in recombination rate of photoinduced carriers. Interlayer charge redistribution is controlled by a substantial increase in occupied orbitals of C_{LL}, empty orbitals of N_{LL}, and localization of FOs relative to *BL-CN*. The interlayer orbital charge transfer $\Delta Q_{il}^{p_x}$, $\Delta Q_{il}^{p_y}$, and $\Delta Q_{il}^{p_z}$ are as follows: 0.035, -0.064 and -0.115 e^-. Table. 5.2 yields ΔQ_{il} of -0.131 e^- upon Li intercalation. The EPP (Fig. 5.10a) and LDOS (Fig. 5.9) confirm the Löwdin charges, where the LL atoms' influence in VB is significantly greater than the UL atoms' contribution, resulting in the formation of $\vec{E_{il}}$ from LL $\rightarrow$ UL; this $\vec{E_{il}}$ is further supported by the placement of Li atom, which is tending closer to UL. As Fig. 5.9(c,d) displays intense states in CB in contrast to p_x/p_y-orbitals, orbital classification further confirms the stimulation of p_z-states for vertical charge transfer. The p_x, p_y, p_z, and s-orbitals of C/N in LL cause significant changes in VB that lead to surface activation, which is advantageous for high reactivity towards OER/HER. The ELF facilitates the decreased interlayer separation, electron localization around the Li atom, increased interlayer orbital

coupling, and increase in the charge variation among UL and LL (Table. 5.2) following Li incorporation as displayed in Fig. 5.10(b,c).

The combination of band edge straddling across reduction-oxidation (redox) potential, visible light absorbance, and reaction feasibility over the surface determines a photocatalyst's potential. Fig. 5.10d shows the parallel, perpendicular component of the absorption coefficient (α) and the imaginary part of the dielectric coefficient (ϵ_2). Due to the narrower band gap of Li-CN and the higher absorption of visible photons, there is a red-shifting of α relative to BL-CN. We have previously reported on the around 3.0 eV curve distortion in im(ϵ_2), which is explained by interlayer orbital overlap. This is seen in the inset. Although it is not visible in the ML, this orbital overlap suggests the activation of the forbidden transition, which offers a broad energy range of photons to excite from VB to CB. It may utilize the whole visible region, as indicated by the several peaks that represent possible transition regions in the visible range of the spectrum. The band edges spanning the redox potential demonstrate how Li-CN may be employed for both OER and HER, as seen in Fig. 5.10e.

5.10 Li-CN Reduction-Oxidation Mechanism

5.10.1 OER and HER Analysis

The head-on orbital overlap between the interlayer atoms maintained with structural relaxation on Li intercalation, and bond formation produced a bridge, as shown in Fig. 5.11a and Fig. 5.10(b, c). In examining the OER/HER across several sites and assessing the overall activity of the Li-CN photocatalyst, the previously reported information that the most electronegative atom is the best site for OER and the greatest e^- donating atom is the best site for HER is taken into consideration. From Fig. 5.11a, it is evident that, out of these sites, N_1, which is considered to be Site 1, N_3, which is considered to be Site 2, and N_2, which is considered to be Site 3, have ΔQ of -0.362, -0.315, and -0.341 e^-, respectively. Concurrently, C_4, representing Site 4, C_5, representing Site 5, and N_5, representing

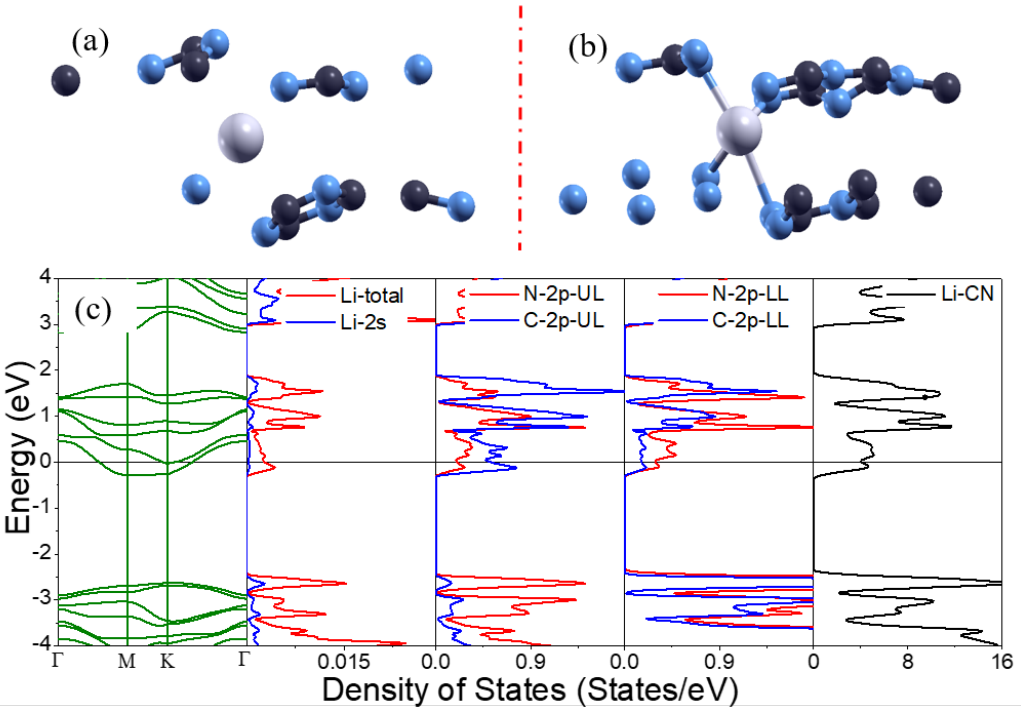

FIGURE 5.8: A side view of the *Li-CN* crystal structure shows the (a) basic and (b) optimized structures; (c) the total, sum of the partial density of states for all atoms in the upper and lower layers of the material, along with bands and the Fermi energy shifted to zero.

Site 6, all had ΔQ values of 0.371, 0.380, and -0.351 e^- and Sites 1, 3, 4, and 2, 5, 6 in the Li-CN structure's UL and LL had been considered to be adsorption sites. Because the sites are electronegative, they have been screened based on the charges accumulated/depleted over either surface of *Li-CN* to test the selectivity of the sites for the adsorption of water molecules over both. Three distinct sites, N_{edge} and C_{corner}, with two N and one C atom, have been considered from any of the layers.

The H_2O relaxation on *Li-CN* for OER reveals an average hydrogen bond (H-bond) of 1.892 Å for $H - N^{edge}$. The average adsorption energy of the H_2O molecule ($\Delta\bar{E}_{ads}^{H_2O}$) over Sites-2, 3, 5, 6, and Sites-1, 4 with $\Delta E_{ads}^{H_2O}$ of $\sim$ -1.01 eV, indicating strong physisorption. To validate *OH interaction with *Li-CN*, energetically stable *OH was estimated for the following step, yielding 1.644 Å of C-OH average bond length and 2.218 Å H-bond (*OH-N^{edge}) for Sites-1,2,3,4,5,6 [158]. Furthermore, the difference in ΔQ_{il} and ΔQ_{Li} is responsible for $\Delta\bar{E}_{ads}^{OH}$, which are -0.079 and 0.608 eV for Sites-1,3,4,5, and 2,6, respectively. The C-O

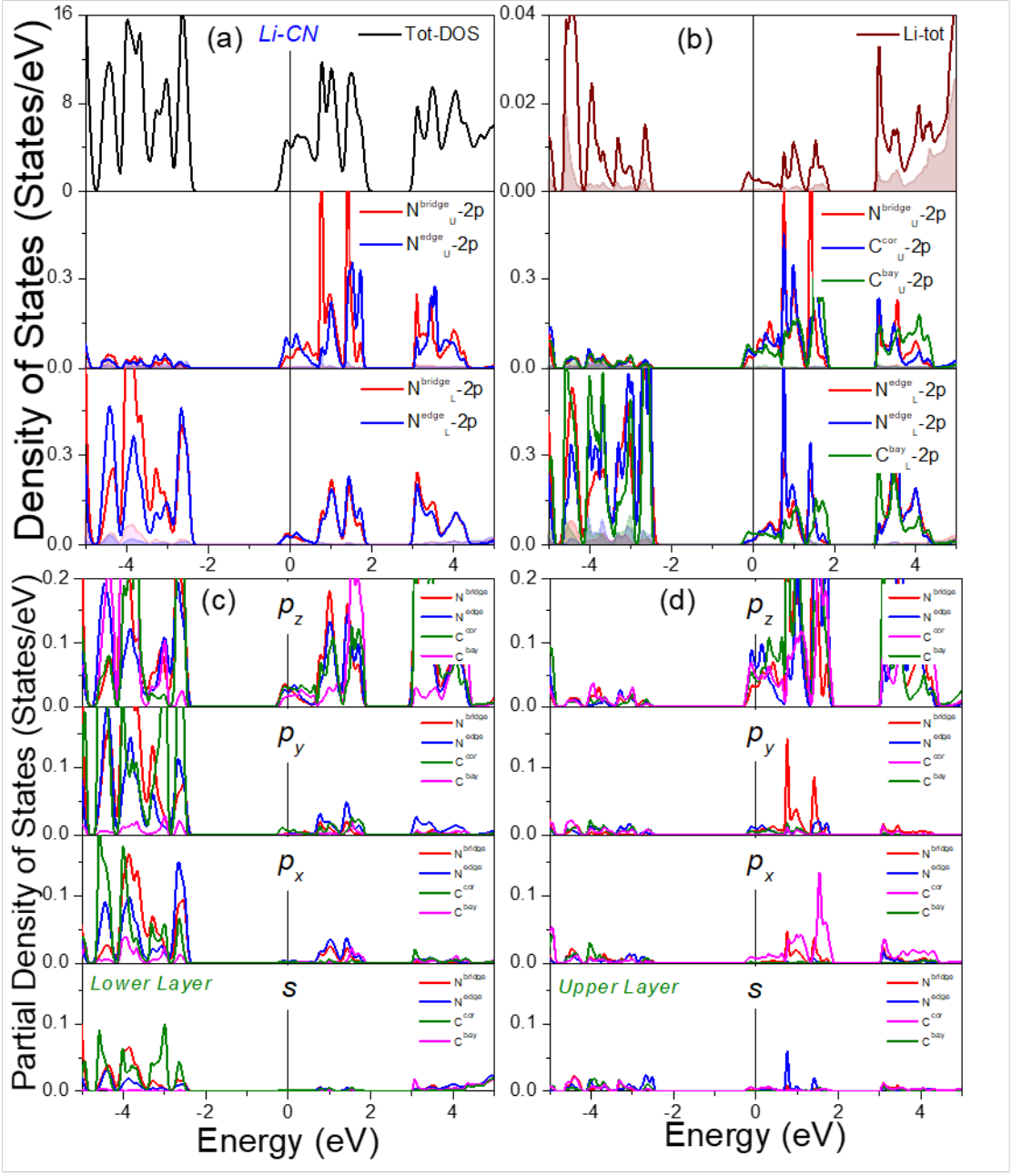

FIGURE 5.9: With Fermi energy shifted to zero, the local and partial density of states for *Li-CN* and atoms involved in interlayer contact via Li bridging.

bond length decreases to $\sim$ 1.296 Å upon H detachment from *OH and with the generation of *OOH it shows $\sim$ 1.508 Å average C-OOH bond length, for the next reaction. *OOH on Sites-1,3,4,6 exhibit an H-bond between $H - N^{edge}$ of around 1.823, whereas Sites-2,5 show no evidence of an H-bond. *OOH at Site-2 has an interlayer N-C bonding-related ΔE_{ads}^{OOH} of 4.569 eV. The establishment of the chemical bond or molecular orbital interaction that drives electron transfer governs reactant adsorption; BL-CN/Li-CN justify $\Delta E_{ads}^{reactant}$ as a function of $\Delta Q_{if}^{reactant}$. Depending on the kind of adsorption, the type of bonding between them, and the polarity of the molecule, the surface contact with the adsorbent produces a distinct interfacial charge redistribution that influences additional charge and reaction kinetics. $\eta^{OER/HER}$ is the result of this $\Delta E_{ads}^{reactant}$, which also influences the change in Gibbs free energy ($\Delta G^{reactant}$). *OH adsorption sites are exothermic; hence, *OH$\rightarrow$*O is the rate-determining step (RDS) for these sites; in contrast, *OOH formation step is the RDS for sites 2-4, where it contributes to the lowest values of ΔQ_{if}^{OH} and $\Delta Q_{p_z}^{OH}$. As can be shown from Fig. 5.11b, η^{OER} values of 0.59, 1.00, 0.76, 0.59, 0.91, and 0.35 V for Sites-1 to 6 demonstrate notable results as an effective photocatalyst.

With an average C-H bond of 1.111Å and $\Delta \bar{E}_{ads}^{H}$ of -0.797 and -0.732 eV for Site-1,4,5,6 and Site-2,3, respectively, $Li - N^{edge}$ bonding in Li-CN promotes H adsorption to C^{corner} and C^{bay}. The largest ΔE_{ads}^{H} is seen at Site-6, where the charge transfer from Li to the $BL - CN$ assembly is the least, at -1.043 eV. The H_3O molecule is adsorbed over identical sites to examine the impact of an additional water molecule's dipole moment [114, 159] on ΔE_{ads}^{H}. While no H-bond is seen between the H_2O molecule and Li-CN, sites 1, 5, and 6 exhibit $\Delta E_{ads}^{H_3O}$ of -0.552, -0.701, and -0.397 eV, respectively, owing to $\sim$ 1.051 Å N-H bond. The reason for the strong chemisorption ($\Delta \bar{E}_{ads}^{H_3O}$ -1.148 eV) at Sites-2,3,4 is the $\Delta \bar{Q}_{if}^{H_3O}$ 0.382 e^-, which is 0.065 e^- greater than at the other sites, and the H-bond between H_2O and Li-CN. As can be shown from Fig. 5.12(a,b), η_H^{HER} and $\eta_{H_3O}^{HER}$ of -0.49 V (Site-2/3) and -0.037 V (Site-6) are within the reduction potential of Li-CN, supporting it as an effective HER catalyst.

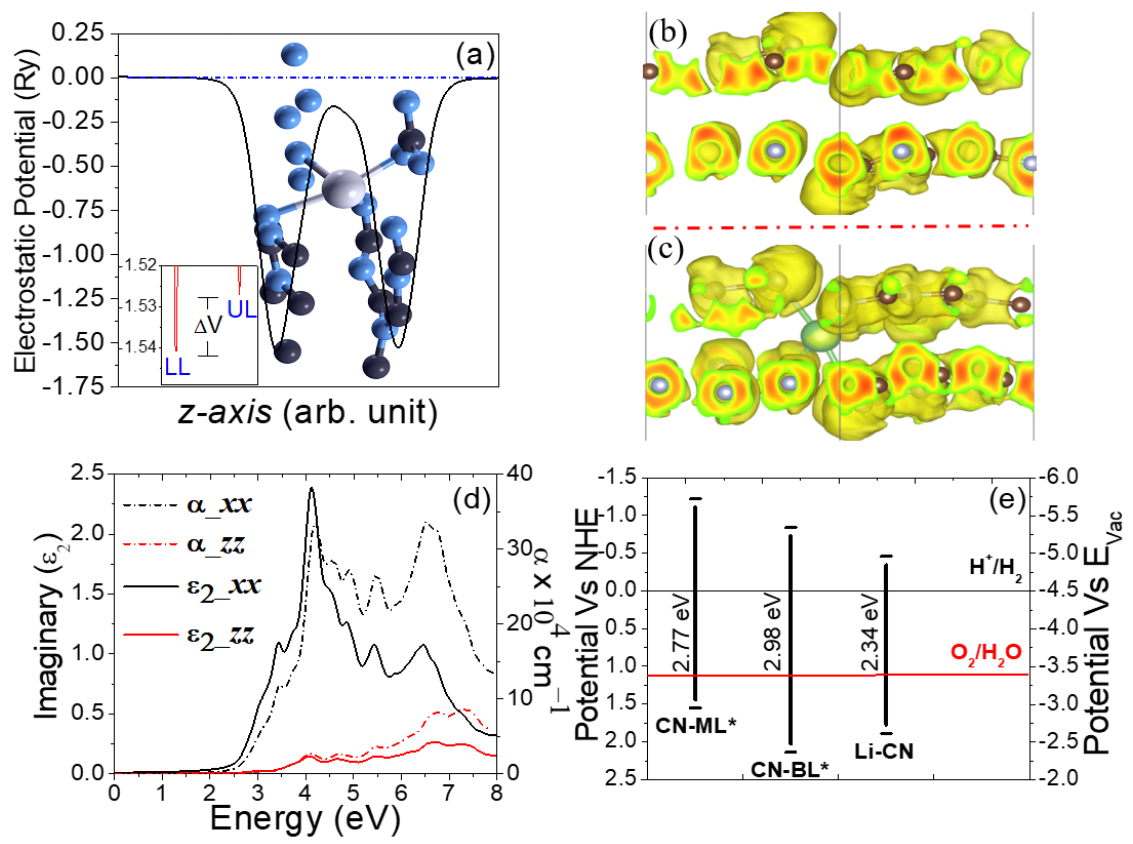

FIGURE 5.10: (a) The electrostatic potential profile illustrates the potential variance with cell length (z-axis). The inset shows how the peak locations of LL and UL vary. Isosurface shows the perspective for (b) *BL-CN*, and (c) *Li-CN* electron localization functions for *Li-CN*. (d) For *Li-CN*, the absorption coefficient (α) & imaginary component of the dielectric function versus energy is shown, with the energy range between 2.6 and 3.8 eV highlighted in the inset, and (e) *BL-CN*, *Li-CN*, and *CN* ML's Reduction-Oxidation potential against the NHE/E_{vac} *[8]

.

Table. 5.3, shows the impact of ΔQ_{il} on the ΔE_{ads} of the subsequent adsorbate. where ΔE_{ads}^{OH} corresponds to low(high) $|\Delta Q_{il}^{H_2O}|$. On the other hand, for Sites-1,2,3,4,5, and-6 (where Li settle in LL on *OOH adsorption), ΔE_{ads}^{O} is inversely proportional to $|\Delta Q_{il}^{OH}|$; this is followed by a linear proportionality between ΔE_{ads}^{OOH} and $|\Delta Q_{il}^{O}|$. It is clear from earlier research that charge transfer between the adsorbent and adsorbate modifies the interface, which in turn controls the reaction's subsequent phase. Interfacial charge transfer (ΔQ_{if}) at the reactant and *Li-CN* interface controls ΔE_{ads}. Moreover, it controls the reactant's ΔG, which adjusts $\eta^{OER/HER}$. Consequently, two main conclusions can be made from this:

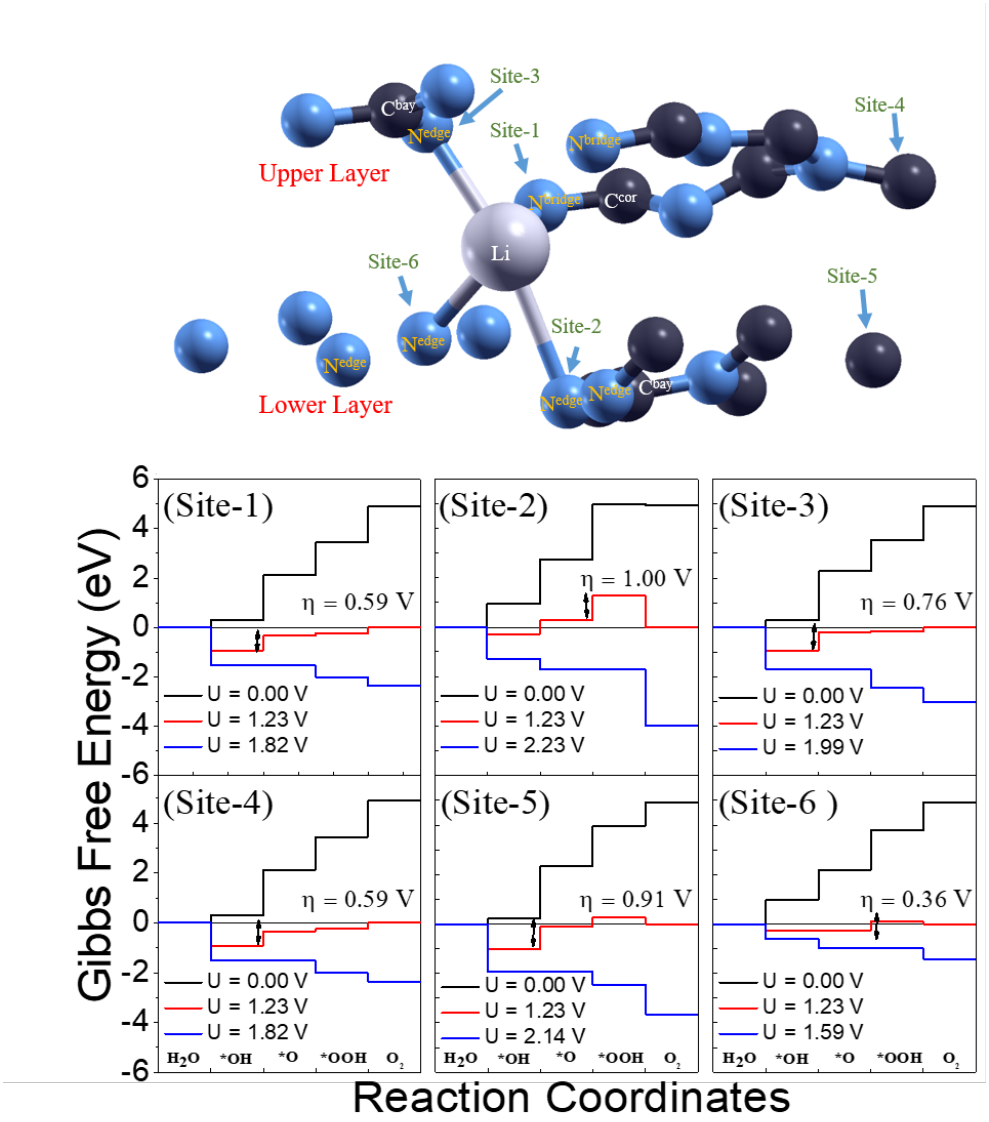

FIGURE 5.11: (a) An enhanced configuration (unit cell) with designated sites for intermediate adsorption; (b) A Gibbs free energy profile for the process of the oxygen evolution reaction, encompassing Sites 1-6 throughout *Li-CN*

(a) interlayer linking during the reaction prefers Li-atom isolation in the void of both layers of *BL-CN*; and (b) ΔQ_{il} / $\vec{E}_{il}$ highly affects ΔE_{ads} of the upcoming reactant, which relies on ΔQ_{if}; hence, coupling between ΔQ_{il} & ΔQ_{if} will naturally govern reactant adsorption."

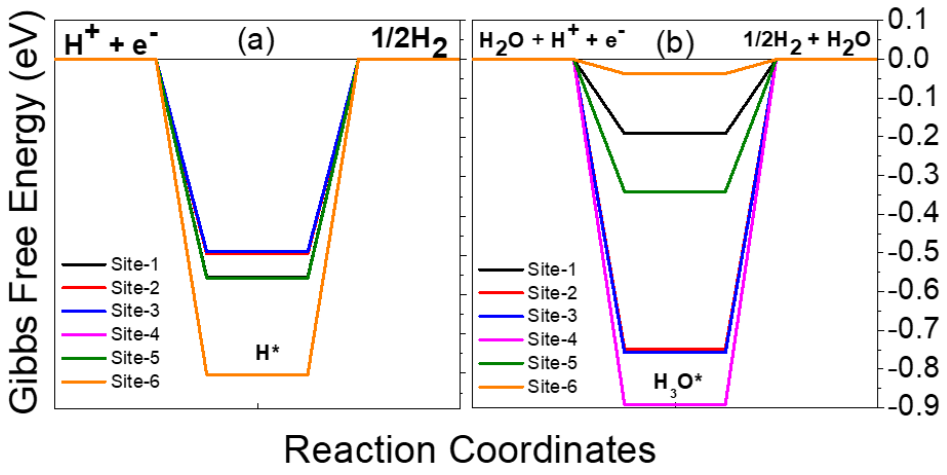

FIGURE 5.12: Profile of Gibbs free energy for the evolution of hydrogen, encompassing Sites 1-6 over *Li-CN*.

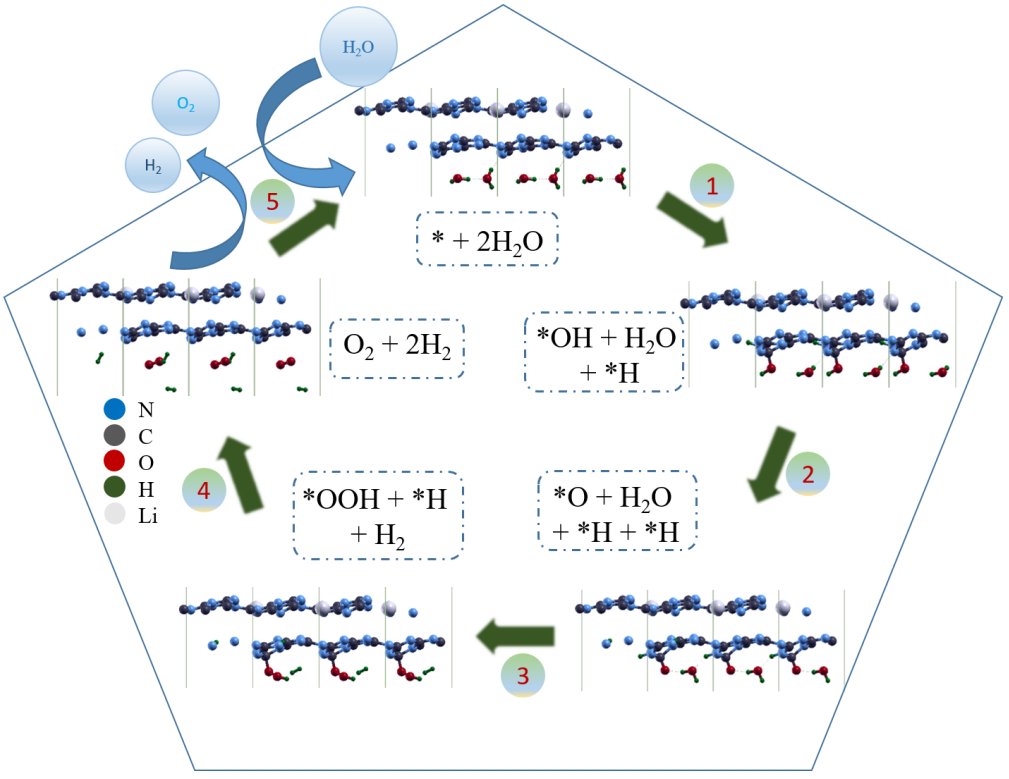

FIGURE 5.13: Sequential oxygen evolution reaction & hydrogen evolution reaction over *Li-CN* in a cyclic process.

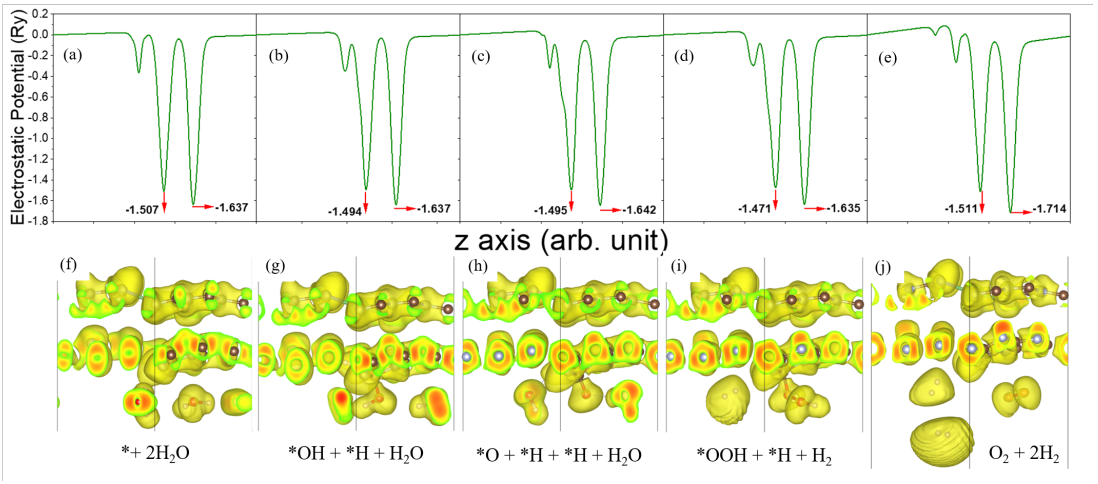

FIGURE 5.14: (a-e) Electrostatic potential plot and, (f-j) ELF for simultaneous OER and HER.

5.10.2 Simultaneous OER and HER

The effects of intermolecular hydrogen bonding over the adsorption energy, charge transfer analysis with multiple atoms consistent throughout the reaction, and simultaneous OER and HER are not studied. We were inspired to design and simulate simultaneous oxygen and hydrogen generation because of the importance of surface termination brought about by OER/HER over the corresponding HER/OER, respectively. When two water molecules are present, the creation of photoanodic (photocathodic) sites on the surface of a photocatalyst will cause oxidation (reduction) and the generation of oxygen (hydrogen). This investigation focuses on the mechanism (Fig. 5.13) to comprehend (i) structural variation based on the charge transfer on reactant adsorption and $E_{ads}^{reactant}$, as well as (ii) correlation between $\vec{E_{il}}$ & $\vec{E_{if}}$ derived from the EPP and individual ELF analysis. As in the previous section when CHE is accomplished without distortion on adsorbent contact, the structural integrity is preserved during the reaction in the simultaneous OER/HER. The OER and HER are initiated simultaneously by the adsorption of two water molecules, leading to the following $\Delta E_{ads}^{H_2O}$ values: -0.635, -0.535, and -0.585 eV for a single H_2O, two H_2O, and H_2O in the presence of another H_2O molecule, respectively (calculated to understand the variation on basis of termination). For $2H_2O$ adsorption, ΔQ_{il} yields -0.676 e^-, which

may be attributed to the electrons' decrement (increment) over LL(UL) and increment over $2H_2O$. Conventionally, $\vec{E_{il}}$ should be created from $LL \rightarrow UL$ and $\vec{E_{if}}$ between $2H_2O \rightarrow Li-CN$ because of ΔQ_{il} and ΔQ_{if}. Li is forced into the CN_{UL} void by $2H_2O$ adsorption, and as a result, $\vec{E_{il}}$ [159] may be observed from EPP, both in terms of magnitude and direction. While the potential difference ($\Delta V = V_{LL} - V_{UL}$) indicates $\vec{E_{il}}$ from $Li-CN_{UL} \rightarrow 2H_2O + CN_{LL}$, it also indicates that the effect of $2H_2O$ adsorbed over Li-CN is governing the effect of $\vec{E_{il}}$ because the direction of $\vec{E_{il}}$ (as seen from ΔQ_{il}) is from LL to UL, which is opposite to the direction of $\vec{E_{il}}$ seen from EPP. We must take into account the function of the newly created interface over the alteration of existing interlayer characteristics since the direction of the electric field on water adsorption over the surface has changed, altering the interfacial properties. The shift in the form of the isosurface to an ellipse for LL and N^{edge} lone pair directed towards the H_2O molecule indicates a significant influence of H_2O on interlayer orbital interaction, given the considerable interlayer separation of the corresponding ELF in comparison to pristine. Extra H_2O interacts with the adsorbed H_2O already present in the process, but it also keeps the resulting $\vec{E_{il}}$ intact when the adsorbed H_2O molecule dissociates in the future. The adsorption and generation of *OH, *H, and H_2O over their respective sites in Step-1 are similar to the previously discussed site selectivity. After N-H, isolated H_2O, C-OH bonding acquires 0.031 e^- because of the HOH-N H-bond, changing ΔQ_{if} in favor of $\vec{E_{if}}$. $H_2O + (H, OH)CN_{LL}/Li-CN_{UL}$ is formed as a result of this ΔQ_{if} (Fig. 5.13, step-1), which lowers the interfacial barrier for quick charge transport and changes $\vec{E_{il}}$. The change in total charge over LL(UL) from the previous phase is the cause of this variance. The values of ΔE_{ads}^{*OH} and $\Delta E_{ads}^{*H^1}$, respectively, show the influence of $\vec{E_{il}}$ on ΔE_{ads}^{*OH}. These values are -0.493 and -1.618 eV. As seen in Fig. 5.14(b, g), this enhances the interlayer orbital interaction. In this case, interlayer distance (potential height) rises (increases), interfacial potential height lowers, and ΔV increases to 0.143 Ry. The system is presented as a surface modified/surface decorated $((OH, H) - CN_{LL}/Li-CN_{UL})$ heterojunction that is advantageous for further deprotonation [139] due to the reduction in the

separation of interlayer distance and the rise in interlayer orbital interaction. The formation of an IvdWH [139] by this surface modification/decoration makes the function of surface termination in the change of interlayer characteristics clear. $\vec{E_{il}}$ varies along with the surface termination (adsorbents), and this variation controls the photoactivity by lowering the energy barrier for the next intermediate adsorption.

In the subsequent stage (Fig. 5.13, step-2), the computed values of ΔE_{ads}^{*O} and $\Delta E_{ads}^{*H^2}$ were determined to be -0.621 and -1.543 eV which explains how linked $\vec{E_{il}}$ & $\vec{E_{if}}$ lowers the barrier height for the subsequent reaction. After the second H release, the Heyrovsky or Tafel mechanism will determine if HER occurs. Rather than removing adsorbed H from the H bound N^{edge}, H decides to bind with N^{edge}, altering the termination to $(2H, O) - CN_{LL}$. ΔQ_{il} for $(2H, O) - CN_{LL}/Li - CN_{UL}$ (Fig. 5.13, step-2) of -0.617 e^- by strengthening the $\vec{E_{il}}$ of the system can facilitate water dissociation and result in viable H_2 desorption via the Heyrovsky or Tafel mechanism. Step-2 further demonstrates that *OH dissociates into *O & *H and their corresponding adsorption, increasing ΔV to 0.147 Ry. It may be shown from Fig. 5.14(c, h) that interlayer distance rises as orbital contact decreases. Although, $\vec{E_{if}}$ increases when the potential dips and the electric field coupling causes an overall increase in the potential difference at either surface (over the adsorbent and $Li - CN_{UL}$). Following water dissociation, C-OOH is formed, and H breaks the connection between H and H to generate a hydrogen molecule (Fig. 5.13, step-3). The disappearing of $\vec{E_{if}}$ and desorption of H_2 are responsible for the high ΔE_{ads}^{OOH} of 3.186 eV. This leads to a decrease in $\vec{E_{il}}$, which is further evidenced by the lowered difference of electric potential from Fig. 5.14d. In Fig. 5.14(d, i), *OOH dip width rises in conjunction with ΔV, and ELF exhibits decreased interlayer separation. Further depletion of O_2 and H_2 molecules results in ΔQ_{il} of -0.606 e^-, which attracts a significant number of H_2O for OER/HER. This may be attributed to further rise (drop) of the total charge of LL (UL) and reduction in ΔQ_{il}. The creation of H_2 & O_2 occurs effectively with the maximum ΔV of 0.203 Ry in Step-4, and the ensuing ELF exhibits properties that are close to those

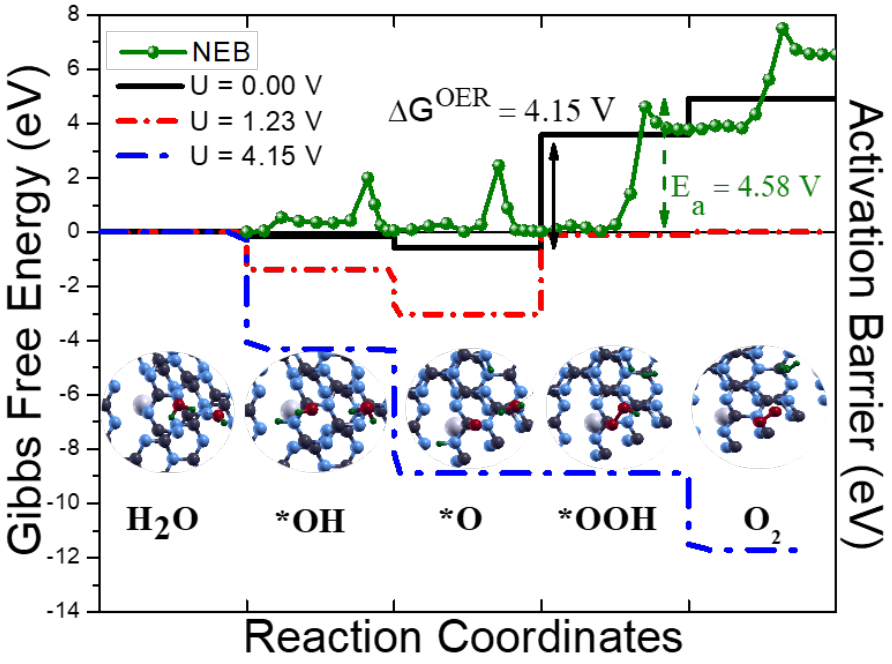

FIGURE 5.15: The *Li-CN* surface is used to accomplish the free energy change for OER and the activation barrier for OER+HER.

of pristine. The dispersion of H_2 and O_2 away from the surface causes a large variance in the total $\vec{E}$. This dispersion leads to (i) no molecule buildup on the surface for H_2O adsorption blocking, and (b) no reverse reaction, which comprises of oxygen reduction reaction over the surface.

Despite the unresolved complexity (limitation of NEB in calculating the E_a for simultaneous OER and HER) of NEB, as shown in Fig. 5.15, NEB formulation for E_a using minimum energy path and free energy change method for potential barrier ($\eta^{OER/HER}$) calculation produced similar findings. We have developed a technique to calculate ΔG^{*OH}, ΔG^{*O}, and ΔG^{*OOH} for two reactions occurring concurrently. The results show that for U = 0.0 V, these values are -0.143, -0.571, and 3.586 eV, respectively. The lowest η^{HER} and $\eta^{OER}(\eta^{OER})$ are determined to be 1.303 V and 2.927 V, respectively. Conversely, NEB confirms that *OOH production is the rate-determining step due to E_a of 4.58 V for $N-H, C-O, N-H, H_2O \rightarrow N-H, C-OOH, H_2$ (Fig. 5.13, step-3). Throughout the water-splitting reaction, variations in E_a and $\eta^{OER/HER}$ follow the same trajectory as at Site-6, which can be attributed to a direct relationship between the $\Delta E_{ads}^{reactant}$ and $\vec{E_{il}}$ (ΔQ_{il}) of its previous step. This relationship is regulated by the $\vec{E_{if}}$ (ΔQ_{if}) caused by

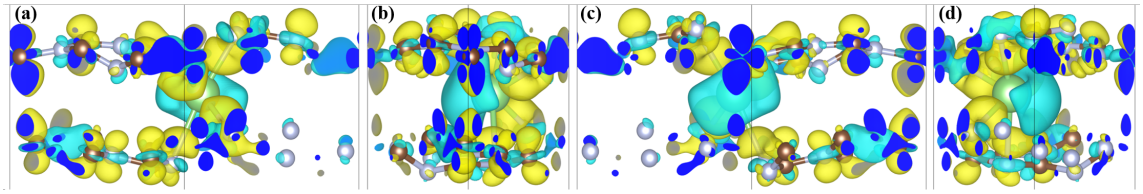

FIGURE 5.16: (a-d) Charge density difference isosurface plot for pristine plotted at different orientations, blue and yellow region indicate charge lost and gained, respectively.

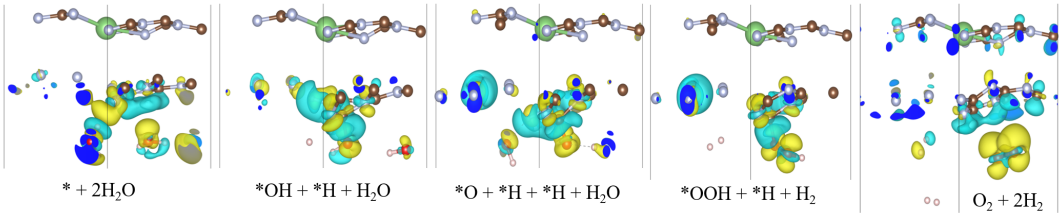

FIGURE 5.17: Charge density difference between the adsorbate and adsorbent Li-CN using $\Delta\rho_1 = \rho_{system} - (\rho_{2H_2O} + \rho_{Li-CN})$

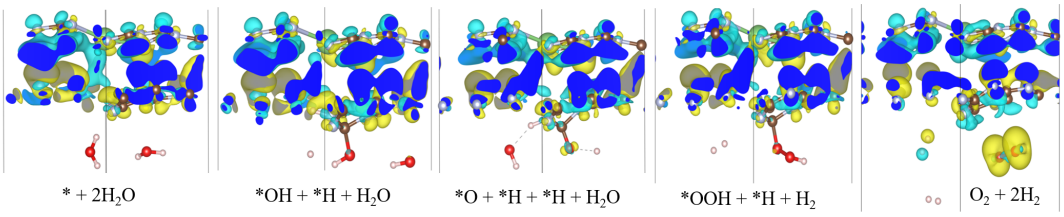

FIGURE 5.18: Charge density difference between the adsorbate over the lower layer and an upper layer with Li using $\Delta\rho_2 = \rho_{system} - (\rho_{2H_2O+CN_{LL}} + \rho_{LiCN_{UL}})$

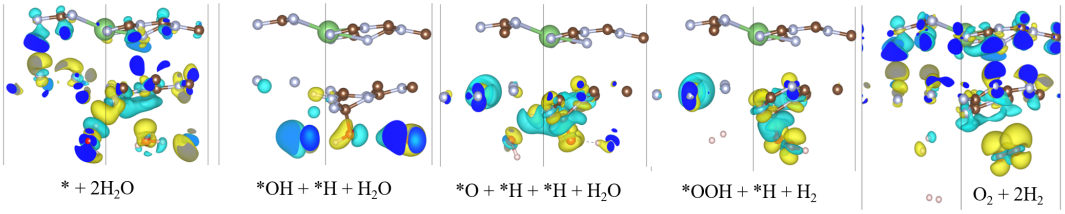

FIGURE 5.19: Charge density difference between the adsorbate, the lower layer, and an upper layer with Li using $\Delta\rho_1 = \rho_{system} - (\rho_{2H_2O} + \rho_{CN_{LL}} + \rho_{LiCN_{UL}})$

reactant adsorption. Site-6 will be chosen for additional water molecule adsorption because it has the lowest overpotential value and dominates site reactivity for OER. This indicates the significance of the electronegative area for appropriate molecule adsorption.

5.11 *Li-CN* Charge Transfer Mechanism

The charge transfer at the adsorbate-adsorbent interface governs the study of the rate-determining step even when the reaction continues with distinct reaction intermediates. Charge transfer investigation from the pristine step is crucial to understanding the parameters required to enhance the photocatalytic activity because the charge transfer mechanism depends on the type of adsorbent, the polarity of the molecule, its interaction with the surface, and the synergistic effect of a surface with its stacked layers. Similar to alkali atom intercalation [28, 139, 142], Li-intercalation generates a potential difference between the stacked layers, which in turn causes the $\vec{E_{il}}$ to form. Band alignment alone will determine the charge following the channel, so potential variations in the adsorption of different chemical intermediates are what explain the creation of IvdWH. These potential differences also explain the interfacial and interlayer charge transfer mechanisms. Figures show charge increase and loss as indicated by the yellow and blue regions, respectively. The charge density difference ($\Delta\rho$) of *Li-CN*, intermediate adsorbed *Li-CN*, is displayed in Figs. 5.16, 5.17, 5.18, and 5.19. For pristine systems, the conventional formalism involving the difference between the charge density of the final system ($Li-CN$) and its component (Li & $BL-CN$) has been taken into consideration. Three techniques have been employed for adsorbed systems to determine the interfacial and interlayer $\Delta\rho$. The blue and yellow regions in Fig. 5.16(a, c) indicate the charge loss from Li and the charge acquired by the Li-N bond, respectively, representing pristine *Li-CN*. The yellow region perpendicular to the surface of *BL-CN* indicates interlayer charge gain, whereas the blue region around the atoms indicates intralayer charge depletion. On $2H_2O$ adsorption, charge obtained by the OH bond and lost by the H atom over H_2O bonded with H-bond is seen, whereas dipole over the other H_2O is observed. The surface in closer proximity to H_2O displays the acquired charge, whereas the same charge is lost across the dipole. In addition to $\vec{E_{if}}$, ρ_2 indicates charge loss over the UL and gain over the LL, which together demonstrates the previously mentioned $\vec{E_{il}}$ (EPP portion). As the reaction continues, changes in $\Delta\rho$ indicate the fluctuation

of the accumulation and depletion region of charges. In Step-1, the charge loss region is shifted towards the N_{edges}-void by *OH and *H, along with the redistribution of $\Delta\rho$ regions for ρ_2 and the decreased dipole of additional H_2O. The $\Delta\rho$ on either side of the surface is influenced by the dense charge differential on *O and *H generated at Step-2, which increases charge loss across the N_{edge} of the void (Fig. 5.18). H_2 detachment vanishes $\Delta\rho$ around it, localizing its impact with less intensity between the surface and *OOH molecule. Nevertheless, a significant difference in Step-3 causes the $\vec{E_{il}}$ to acquire strength. The coupling between $\vec{E_{if}}$ and $\vec{E_{il}}$ is finally justified in Step-4 by O_2 with a substantial charge gain when it is desorbed together with H_2 leaving CN_{LL} with charge depletion region, and for ρ_2 obvious charge accumulation/depletion pairing at both the interface. Li-CN exhibits 0.56 V, or $\sim$ 4.1 and $\sim$ 2.05 times reduction, respectively, for the oxygen evolution process, with an overpotential of 2.32 V and 1.15 V over ML- and BL-CN, respectively. In the meanwhile, Li-CN exhibits a $\sim$ 3.4 times decrease and a $\sim$ 4 times increase from ML and BL-CN, respectively, for the overpotential of the hydrogen evolution process. In contrast to ML-, BL-CN, Li-CN exhibits superiority due to its overpotential within the band edges, which directs the potential for total water splitting.

5.12 Conclusion

Hybrid DFT has been used to analyze and present the study of structural, electronic, optical, and photocatalytic properties of ML and spatially tailored BLs, as well as reaction kinematics for a significant photoactive bilayer (S_3) covering all the steps involved in the photocatalytic process. The problem of π-localization in ML CN is solved by band gap tuning because of structural changes in BLs, increased spatial charge distribution, and higher electron mobility; but, the problem of rapid photogenerated $e^- - h^+$ pair recombination is solved by S_3 configuration of BL because of interlayer $\pi - LP$ hybridization, which also increases the absorption in the visible region for BLs. The water dissociation reaction is the limiting step for all OER sites, according to charge transfer studies and the formation of an $\vec{E_{if}}$

on adsorption, whereas the influence of additional H_2O on lowering the value of free energy change for highly efficient HER. Charge accumulation and dispersion at the edges strengthen the ability of reaction sites due to in-plane π-conjugation driven by interlayer orbital interaction. This is evident from the decrease in the adsorption energy of intermediates, which results in a modification of the overpotential with values of -1.15 V for OER and -0.20 V (-0.05 V with additional H_2O molecule) for HER enhanced photoactivity compared to ML, and navigates up possibilities for its application in flexible nano-devices for complete water splitting that produces hydrogen fuel even at the nanoscale.

The lack of an intercalant, which prevents effective charge transfer across the bilayer before illumination and intermediate adsorption, is one of the problems with BLs. Li is intercalated in the $BL-CN$ to solve this problem. Li intercalation has an impact on the system's charge transfer mechanism and the development of a charge transfer channel between the CN layers. Between the upper and lower layers of CN, intercalation of Li produces an $\vec{E_{il}}$, and as the reaction progresses, reactant contact with the photocatalyst surface produces an $\vec{E_{if}}$. The $\vec{E_{if}}$ and the produced $\vec{E_{il}}$ pair to promote effective reactant adsorption. Li-mediated $BL-CN$ bridging modifies the optical and electrical characteristics. Because of this, Li-CN is a more effective photocatalyst than BL-CN because of its high absorbance in the visible region, band edge straddling of the reduction-oxidation potential, and variation in $\vec{E_{il}}$, $\vec{E_{if}}$, and $\Delta E_{ads}^{reactant}$ as the reaction progresses. The significance of two H_2O molecules is also highlighted in this study to comprehend the charge transfer channel and simultaneous HER and OER reaction mechanism.